Where did the Arizona-plano go? Protracted thinning via upper- to lower-crustal processes

Gilby Jepson[*1], Barbara Carrapa[1], Sarah W. M. George[1], Lauren J. Reeher[1], Paul A. Kapp[1], George H. Davis[1], Stuart N. Thomson[1], Chiara Amadori[1, 2], Chris Clinkscales[1], Sean Jones[3], Andrew J. W. Gleadow[3], and Barry P. Kohn[3]

[1] *Department of Geosciences, University of Arizona, Tucson, Arizona, USA*

[2] *University of Pavia, Department of Earth and Environmental Sciences, Pavia, Italy*

[3] *School of Geography, Earth and Atmospheric Sciences, University of Melbourne, Melbourne, Victoria, 3010, Australia*

March 24, 2022

Abstract

Mesozoic-Cenozoic subduction of the Farallon slab beneath North America generated a regionally extensive orogenic plateau in the southwestern US during the latest Cretaceous, similar to the modern Central Andean Plateau. In Nevada and southern Arizona, estimates from whole-rock geochemistry suggest crustal thicknesses reached ~60-55 km by the Late Cretaceous. Modern crustal thickness is ~28 km, requiring significant Cenozoic crustal thinning. Here, we compare detailed low-temperature thermochronology from the Catalina metamorphic core complex (MCC) to whole rock Sr/Y crustal thickness estimates across southern Arizona. We identify three periods of cooling. A limited cooling phase occurred prior to ~40 Ma with limited evidence of denudation and ~10 km of crustal thinning. Major cooling occurred during detachment faulting and MCC formation at 26-19 Ma, corresponding to ~8 km of denudation and ~8 km of crustal thinning. Finally, we document a cooling phase at 17-11 Ma related to Basin and Range extension that corresponds with ~5 km of denudation and ~9 km of crustal thinning. During the MCC and Basin and Range extension events, the amount of denudation recorded by low-temperature thermochronology can be explained by corresponding decreases in the crustal thickness. However, the relatively limited exhumation prior to detachment faulting at ~26 Ma

[*]corresponding author (gjepson@arizona.edu)

recorded by thermochronology is insufficient to explain the magnitude of crustal thinning (~10 km) observed in the whole rock crustal thickness record. Therefore, we suggest that crustal thinning of the Arizona-plano was facilitated via ductile mid- to lower-crustal flow, and limited upper-crustal extension at 50-30 Ma prior to detachment faulting and Basin and Range extension.

1 Introduction

Regions of high-elevation and thick crust define many of the Earth's active contractional tectonic settings. Shortening thickens the crust and, if a landscape is in isostatic equilibrium, creates high elevation (e.g. England & McKenzie 1982, Zhong 1997). Modern orogenic plateaus are found in Tibet, South America, and Anatolia, and can influence plate motions and the Earth's climate (e.g. Ruddiman & Kutzbach 1991, Molnar et al. 2010, Schildgen et al. 2012, Wu et al. 2014, Botsyun et al. 2016). The height and relief of such plateaus are controlled by both upper-crustal structures and lower-crustal processes (e.g. Chengfa et al. 1986, Wernicke 1990, Bird 1991, Royden et al. 1997), thus, we consider both when interrogating the formation and ultimate demise of orogenic plateaus. In the western USA, protracted Late Jurassic - Early Cretaceous subduction of the Farallon plate generated shortening related structures in the Sevier fold-thrust belt and Laramide basement-block uplifts with extreme crustal thickening concentrated in the hinterland, leading to the development of an orogenic plateau (Figure 1, e.g., Saleeby 2003, DeCelles 2004, Dickinson 2004, Yonkee & Weil 2015). The regionally extensive plateau likely extended from northern Nevada to southern Arizona and even northern Mexico (DeCelles 2004, Chapman et al. 2015, Bahadori et al. 2018, Chapman et al. 2020). Presently, the western US is defined by relatively thin crust (e.g. Gilbert 2012), thus presenting an opportunity to investigate the processes behind orogenic plateau demise.

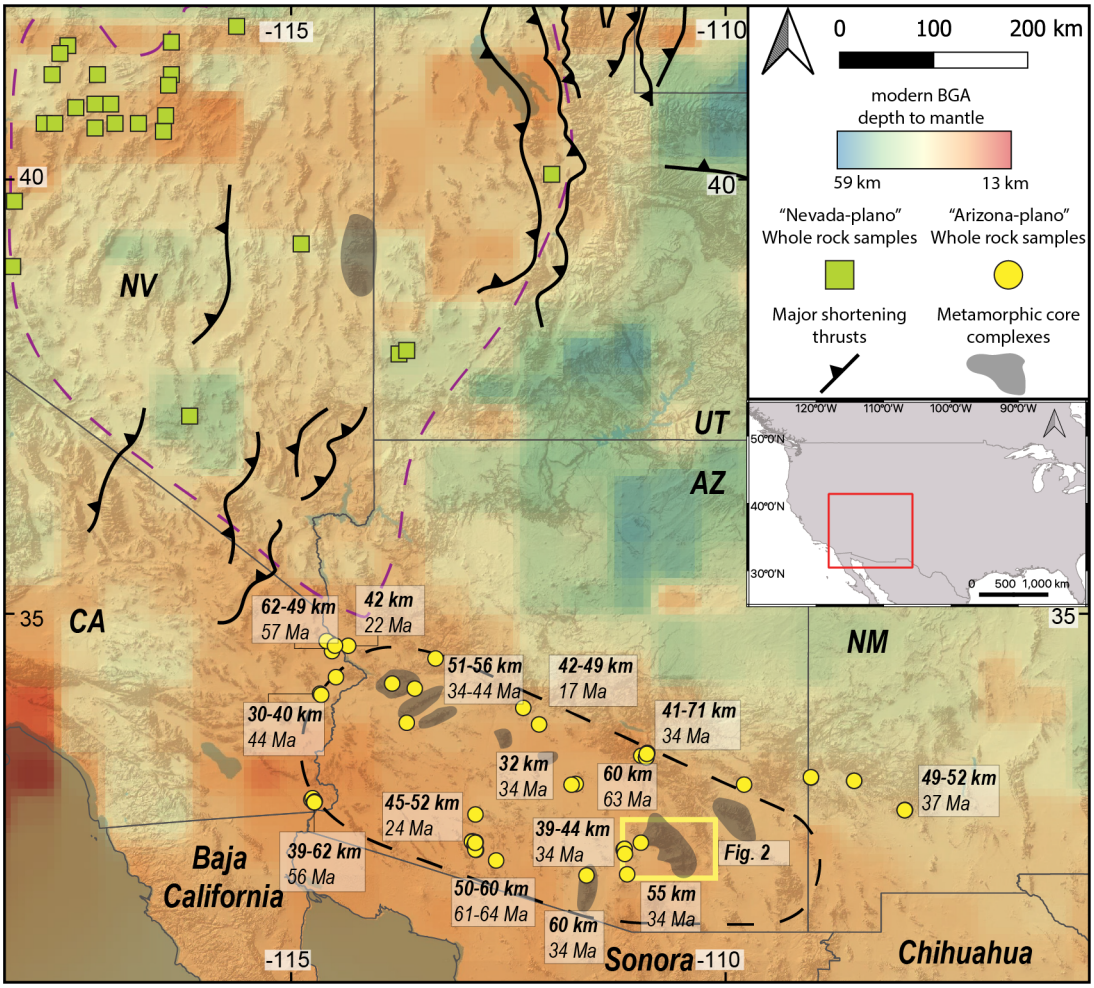

Figure 1: Map of the south-western USA and north-western Mexico highlighting the “Nevada-plano" (purple dashed outline), “Arizona-plano" (black dashed outline), whole rock crustal thickness estimates and associated ages, and major shortening structures from Yonkee & Weil (2015). Modified after (Chapman et al. 2015, 2020). Estimated depth to mantle is from the Bouguer Gravity Anomaly (BGA, Gilbert 2012).

Crustal thinning is required for orogenic plateau demise. In regions where extension is concentrated along discrete, corrugated low-angle normal faults (also known as detachment faults), ductile rocks may be exhumed to the surface and define a metamorphic core complex (MCC, e.g. Coney & Harms 1984, Lister & Davis 1989, Rey et al. 2009, Whitney et al. 2013, Platt et al. 2015). A discontinuous north-south trending belt of MCCs in the western North American Cordillera has been related to extension and collapse of overthickened crust (e.g. Davis 1987). In the south-western North American Cordillera, the belt of these MCCs trend NW-SE from southeastern California into Sonora, Mexico. In southeastern Arizona, the Catalina-Rincon MCC (Catalina MCC, e.g. Davis 1987) is presently underlain by crust that is ~28 km thick (Figure 1, Frassetto et al. 2006, Gilbert 2012). Geochemical data from *ca.* 70-50 Ma plutons in the Catalina MCC, however, suggest that the crust at this locality reached thicknesses of

~60 km during the Late Cretaceous (Chapman et al. 2020), suggesting a ~50 % reduction in crustal thickness. Thus, the Catalina MCC provides an opportunity to investigate the processes at play during crustal thinning/redistribution associated with orogenic collapse.

A shift from fast and perpendicular convergence in the Cretaceous-Paleogene to slower and more oblique convergence in the Eocene allowed gravitational collapse of the thickened orogenic crust (e.g. Livaccari 1991, Copeland et al. 2017). Three dominant mechanisms have been proposed for thinning the crust in this type of setting: 1) upper-crustal horizontal extension; this would predict significant rock cooling as a result of tectonic exhumation, 2) erosion denudation of near surface rocks, which would also result in rock cooling, and 3), ductile flow of mid- to lower- crust with limited or localized upper-crustal extension or erosion and hence only limited rock cooling recorded by low-temperature thermochronometers (e.g. Braun et al. 2006). In this study, we integrate apatite and zircon fission-track (AFT and ZFT) and apatite and zircon (U-Th-Sm)/He (AHe and ZHe) thermochronology data from the Catalina MCC with published whole rock Sr/Y ratios to document periods of crustal thinning and denudation (Table 1 and Figure 2) and evaluate the underlying driver(s).

Table 1: Samples collected from the Catalina-Rincon metamorphic core complex. Age is the reported crystallization age of the rock, “Lat" is the north latitude and “Long" is the east longitude using coordination system WSM 84, elevation (Elev) in meters above sea level. AFT is apatite fission-track, ZFT is zircon fission-track, AHe is apatite (U-Th-Sm)/He, and ZHe is zircon (U-Th-Sm)/He. Samples in italics are from Jepson et al. (2021).

Sample	Method	Lithology	Age	Lat	Long	Elev. (m)
PR-01	ZFT	Wilderness Granite Suite	Eocene	32.372	-110.939	1660
PR-02	ZFT	Wilderness Granite Suite	Eocene	32.370	-110.944	1357
PR-03	ZFT	Wilderness Granite Suite	Eocene	32.373	-110.948	1062
Tort-01	AFT	Catalina Granite	Oligocene	32.477	-111.127	779
Tort-02	AFT	Catalina Granite	Oligocene	32.493	-111.096	1032
Tort-03	AFT	Pinal Schist	Proterozoic	32.512	-111.076	1024
SP-01	AFT/AHe/ZHe	Oracle Granite	Proterozoic	32.399	-110.689	2258
WP-01	AFT/AHe/ZHe	Wilderness Granite Suite	Eocene	32.367	-110.718	2004
LM-02	AFT/ZHe	Wilderness Granite Suite	Eocene	32.359	-110.726	1470
SC-01	AFT/AHe/ZHe	Wilderness Granite Suite	Eocene	32.332	-110.718	1642
GM-02	AFT	Diabase	Cretaceous	32.344	-110.327	1152
UoM0522-01	AFT/AHe	Wilderness Granite Suite	Eocene	32.353	-110.722	1642
UoM0522-02	AFT/AHe	Wilderness Granite Suite	Eocene	32.339	-110.715	1491

UoM0522-03	AFT/AHe	Wilderness Granite Suite	Eocene	32.338	-110.690	1336
UoM0522-04	AFT/AHe	Oracle Granite	Proterozoic	32.321	-110.707	1164
UoM0522-05	AFT/AHe	Wilderness Granite Suite	Eocene	32.257	-110.721	933
UoM0522-06	AFT/AHe	Wilderness Granite Suite	Eocene	32.322	-110.851	888
UoM0422-02	AFT/AHe	Wilderness Granite Suite	Eocene	32.372	-110.948	1003
UoM0422-03	AFT/AHe	Wilderness Granite Suite	Eocene	32.405	-110.910	921
UoM0422-04	AFT/AHe	Catalina Granite	Oligocene	32.437	-110.879	983
UoM0422-05	AFT/AHe	Oracle Granite	Proterozoic	32.310	-110.741	932
UoM0422-06	AFT/AHe	Oracle Granite	Proterozoic	32.307	-110.719	1085
UoM0422-07	AFT/AHe	Wilderness Granite Suite	Eocene	32.330	-110.693	1292
UoM0422-09	AFT/AHe	Wilderness Granite Suite	Eocene	32.377	-110.696	2071
UoM0422-10	AFT/AHe	Wilderness Granite Suite	Eocene	32.444	-110.761	2392
UoM0422-12	AFT/AHe	Wilderness Granite Suite	Eocene	32.401	-110.699	2291
UoM0422-13	AFT/AHe	Oracle Granite	Proterozoic	32.342	-110.907	1060
UoM0422-14	AHe	Oracle Granite	Proterozoic	32.351	-110.942	969
UoM0422-15	AFT/AHe	Johnny Lyon granodiorite	Proterozoic	32.060	-110.663	1094
UoM0422-17	AFT/AHe	Wilderness Granite Suite	Eocene	32.140	-110.616	1049
KJJ09-03	*AFT*	*Wilderness Granite Suite*	*Eocene*	*32.354*	*-110.723*	*1608*
KJJ09-07	*AFT*	*Leatherwood Granodiorite*	*Cretaceous*	*32.452*	*-110.752 2337*	
KJJ09-08	*AFT*	*Rice Creek Porphyry*	*Cretaceous*	*32.479*	*-110.697*	*1049*

2 Tectonic setting

The North American Cordillera extends from Alaska to Mexico and formed in response to Mesozoic-Cenozoic subduction of the Farallon plate underneath the North American continent (e.g. Oldow et al. 1989, DeCelles 2004). Subduction of the Farallon plate generated two major phases of shortening and deformation which overlapped spatially and temporally (Burchfiel et al. 1992, Dickinson 2004, Yonkee & Weil 2015): 1) The Sevier fold-thrust belt, characterized by thin-skinned deformation of Proterozoic through Mesozoic sedimentary sequences (DeCelles 2004, Yonkee & Weil 2015), and 2) the Laramide province, characterized by high-angle, basement-involved reverse faults mostly reactivating pre-existing basement structures (e.g. Dickinson & Snyder 1978, Dickinson 2004). Both events occurred due to sub-

duction of the Farallon Slab and its switch from high-angle subduction (Sevier) to low-angle subduction (Laramide) due to either subduction of a buoyant plateau or ridge (e.g. Saleeby 2003, Humphreys 2009, Liu et al. 2010) or to basal traction (Bird 1998). These tectonic events resulted in widespread deformation, magmatism, and crustal thickening across western North America (e.g. Snyder et al. 1976, Sonder & Jones 1999, Yonkee & Weil 2015).

The Laramide tectonic event is associated with a phase of crustal thickening in the North American Cordillera hinterland (Bird 1998, Yonkee & Weil 2015). Thermochronometric ages from basement exposed within Wyoming and the Colorado Plateau suggest that Laramide shortening in the SW North American Cordillera initiated at *ca.* 80 Ma and intensified at *ca.* 60 Ma (e.g. Flowers et al. 2007, Peyton & Carrapa 2013, Fan & Carrapa 2014, Winn et al. 2017, Copeland et al. 2017, Rønnevik et al. 2017, Scoggin et al. 2021). In Arizona, Laramide shortening is suggested to have caused crustal thicknesses to reach ~50-60 km (Chapman et al. 2015, 2020). In the northern portions of the North American Cordillera, shortening was followed by the onset of slab-roll back at *ca.* 50-40 Ma, recorded by the creation of metamorphic core complexes, extensional basin development and felsic magmatism (e.g. Barton 1990, Wells & Hoisch 2008, Best et al. 2009, Yonkee & Weil 2015, Best et al. 2016, and references therein) which swept southward from southern Canada, causing an increase in rock cooling and exhumation (Fan & Carrapa 2014, Copeland et al. 2017). However, in Arizona and New Mexico it has been proposed that the slab-roll back did not occur until $\leq$ 40 Ma (e.g. Coney & Reynolds 1977, Thacker et al. 2021).

Following foundering and subsequent rollback of the Farallon slab, the thickened North American crust of the SW North American Cordillera then underwent two major phases of Paleogene-Neogene extension (e.g. Lerch et al. 2007). Initially, there was a period of low-angle detachment faulting which exposed lower-plate igneous and metamorphic rocks, followed by a second period of high-angle block faulting forming the Basin and Range (Dickinson 1991). The major phase of extension associated with slab-roll back in southern Arizona was accommodated by large-scale detachment faulting and exhumation of MCCs. In southern Arizona, the onset of MCC detachment faulting varies between *ca.* 30 and 20 Ma (e.g. Gottardi et al. 2020). The onset of detachment faulting gets younger northward from northern Mexico (from 35 to 20 Ma) central Arizona and southward from south-eastern California (from 24 to 20 Ma) to central Arizona (Gottardi et al. 2020, and references therein). The Catalina MCC is controlled by the Catalina detachment fault (Figure 2; Dickinson 1991), with fault initiation dated at *ca.* 26 Ma from fault-tilted ash-flow tuffs (Peters et al. 2003) and had ceased by *ca.* 20 Ma (Fayon et al. 2000). The Catalina detachment fault cuts late Proterozoic and Paleozoic sedimentary, metasedimentary, and

igneous rocks, exposing the igneous and metamorphic rocks which comprise the footwall of the detachment (e.g. Fornash et al. 2013). The footwall forms the Catalina MCC edifice and is predominately comprised of Paleoproterozoic Pinal Schist, Mesoproterozoic Oracle Granite, the Paleocene-Eocene Wilderness Suite Granite (Arca & Johnson 2010), as well as Cretaceous and Paleogene intrusions (e.g. Fornash et al. 2013, Spencer et al. 2019, Ducea et al. 2020). Exposed basement closest to the Catalina detachment hosts pervasive deformation indicative of greenschist to amphibolite metamorphism forming the Oracle and Wilderness mylonite (Davis 1987, Spencer & Reynolds 1989, Spencer et al. 2019).

Oligocene thinning via low-angle detachment faults transitioned into high-angle normal faulting throughout the Basin and Range extension, when the relative motions between the North American and Pacific plates led to widespread block faulting via extension throughout western North America (Dickinson 1991). In southern Arizona, Basin and Range extension initiated at *ca.* 18 Ma and continued into the Pliocene, the bulk of Basin and Range extension occurred between 15 and 12 Ma (Dickinson 1991). The Basin and Range extension dissected the ductile MCC detachment faulting, and generated high-relief cliffs which are observed in the range today (e.g. Fayon et al. 2000, Davis et al. 2004). The most prominent local Basin and Range structure in the study area is the Pirate Fault, which cross-cuts the core complex detachment fault on the northwestern extent of the Catalina MCC (Figure 2).

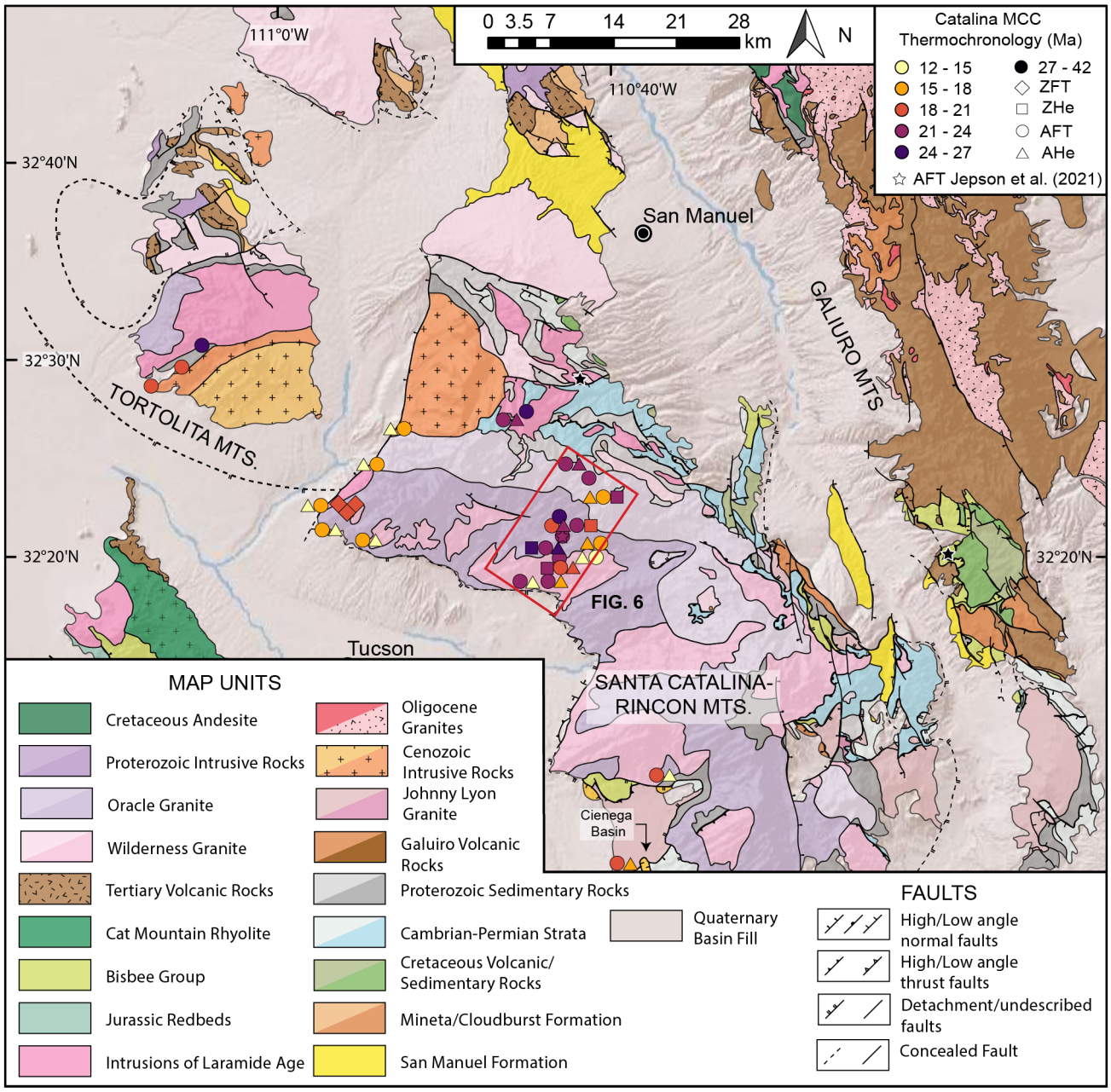

Figure 2: Geological map of the Catalina-Rincon metamorphic core complex (MCC) indicating major structures and units after (Arca & Johnson 2010), apatite fission-track (AFT), zircon fission-track (ZFT), apatite (U-Th-Sm)/He (AHe), and zircon (U-Th-Sm)/He (ZHe) ages from this study and (Jepson et al. 2021).

3 Methods

Thirty-one samples were obtained from exposed crystalline basement comprising the footwall of the Catalina detachment (Figure 2). Samples were collected in an elevation profile perpendicular to the trace of the Catalina detachment, along high-angle normal faults which cut the Catalina detachment, as

well as within the complex network of faults which lie to the east of the main Catalina MCC edifice (Figure 2).

3.1 Zircon and Apatite fission-track

The fission-track thermochronometer relies on the spontaneous fission decay of ^{238}U (Hurford & Green 1983). Spontaneous fission within zircon is annealed above ~280 - 200 °C and above ~120 - 60 °C within apatite, making these systems useful for constraining upper-crustal cooling (e.g. Braun et al. 2006, and references within). Zircon crystals were mounted in Teflon and etched in a NaOH-KOH eutectic melt at 220 °C for 32-62 hours (Gleadow et al. 1976). The optimum etch time for zircon is calculated based on age and radiation damage and was checked by several etching and observation steps at 3-10 hour time intervals. Apatite crystals are mounted in epoxy and polished, with spontaneous fission-tracks revealed through etching with 5.5M nitric acid for 20 s at 21 °C before irradiation (after Donelick et al. 2005). Samples were analyzed via external detector method (Gleadow et al. 1976) which utilizes low uranium muscovite mica detectors, and were irradiated at the Oregon State University Triga Reactor, Corvallis, USA and the Hifar Reactor at Lucas Heights, Australia. The total neutron fluence was checked using CN5 U-doped glass for the apatite samples, and European Institute for Reference Materials and Measurements (IRMM) uranium-doped glass 541 for zircon samples.

Following irradiation, the mica sheets were etched in 40% hydrofluoric acid for 45 min at 21 °C (after Donelick et al. 2005). Zircon and apatite fission-tracks were counted by using an Olympus BX51 microscope with an associated digitizing tablet and computercontrolled stage (Kinetek) in Tucson and a Zeiss AxioTron microscope with Zeiss Scanning Stage under FT Stage control in Melbourne. The fission-track analyses were performed at the University of Arizona Fission Track Laboratory and the Melbourne Thermochronology Laboratory (Table 2 and Supplementary Table 1-2). Confined fission track length distributions were obtained to determine cooling rates, mean track lengths (MTLs) of > 13.5 μm can be considered reflective of rapid cooling (Ketcham et al. 2007). The central ages were calculated by using the ζ-method after Hurford & Green (1983) (Tables 2).

3.2 Zircon and Apatite (U-Th-[Sm])/He

The (U-Th-Sm)/He thermochronometer relies on the accumulation and thermally activated diffusion of radiogenic ^{4}He. The closure temperature for AHe is typically between ~80–40 °C and for ZHe below ~180

°C, thus it is valuable for determining middle- to upper-crustal cooling (Reiners 2005). The apatite helium analyses were performed under two different conditions, samples labelled UoM were obtained from the University of Melbourne following the protocols described in Spiegel et al. (2009). Whereas apatite and zircon analyses without this label were undertaken at the Arizona Radiogenic Helium Dating Laboratory at the University of Arizona and followed the protocols described in Reiners (2005).

For samples labelled “UoM", apatite crystals were picked using the guideline of Farley (2002) at the University of Melbourne. Helium (^{4}He) was extracted in a furnace under vacuum at 870 °C and measured through isotope dilution using a quadrupole ICP-MS (Spiegel et al. 2009). The U-Th-Sm data which was used in age calculation was acquired through total dissolution in HNO_3 of degassed apatite and analyzed by a quadrupole ICP-MS. Replicate analyses of Durango apatite was used as an internal standard (n = 10) measured throughout this study, yielded mean (U-Th-Sm)/He ages of 30.5 $\pm$ 1.4 Ma (1σ), in agreement with the reference Durango (U-Th-Sm)/He age of 31.02 $\pm$ 1.01 Ma (McDowell et al. 2005).

Helium (^{4}He) was extracted at 900-1300 °C, under ultra-high vacuum with a diode laser and measured via isotope dilution on an Element 2 mass spectrometer at the University of Arizona. Following ^{4}He extraction, tubes which contained apatite and zircon were retrieved from the laser cell, then spiked with ^{235}U and ^{230}Th and dissolved. Blank, Sample, as well as spiked standard solutions were subsequently analyzed via isotope dilution for ^{238}U and ^{232}Th, and then with an external calibration for ^{147}Sm via ICP-MS (Reiners 2005). Replicate analyses of Durango apatite were performed as an internal standard (n = 7) yielded a mean (U-Th-Sm)/He age of 31.5 $\pm$ 0.5 Ma (1σ), consistent with the Durango (U-Th-Sm)/He reference age of 31.02 $\pm$ 1.01 Ma (McDowell et al. 2005). Replicate analyses Fish Canyon Tuff zircon were used as an internal standard (n = 2) yielded a mean (U-Th-Sm)/He age of 28.4 $\pm$ 0.8 Ma (1σ), consistent with the Fish Canyon Tuff (U-Th-Sm)/He reference age of 28.3 $\pm$ 0.8 Ma (Gleadow et al. 2015).

3.3 Whole rock crustal thickness estimates

We employed an empirical relationship between igneous whole-rock Sr/Y and Moho depth to estimate crustal thickness through time, as outlined in Chapman et al. (2015). The application of geochemical data to estimate crustal thickness is based on the observation that the trace element signature of subduction related magmas is correlated with certain crustal proxies (e.g. crustal thickness). Specifically, Sr/Y ratios

have been found to correlate with crustal thicknesses at global scales (Best et al. 2009, Lee & Morton 2015). This geochemical discrimination is possible as Sr is preferentially sequestered by plagioclase at low pressures, whereas at high pressures, plagioclase crystallization is suppressed, and Sr enters the liquid phase (Mantle & Collins 2008). In comparison, Y enters the liquid phase at low pressures and partitions into garnet at high-pressure (Chapman et al. 2015). Thus, increasing ratios of whole rock Sr/Y correlate with magmas which form at greater depth, and thus in thicker crust. However, these empirical relationships break down in rocks with >68 wt % and < 55 wt % SiO_2, MgO content of < 4 wt %, and Rb/Sr ratios of between 0.05 and 0.25 (Chiaradia 2015, Chapman et al. 2015, 2020, and references therein). These constraints require filtering of rocks that are either too mafic or too felsic (S-type granitoids), as well as rocks that are altered. Samples (n = 71) analyzed in this study were queried from the NAVDAT database, are located in southern Arizona-western New Mexico and range in age from 68-16 Ma (Figure 1). Sample information, geochemical data for compiled analyses, and crustal thickness estimates are presented in Supplementary File 4.

3.4 Thermal History Modelling

Thermal history modelling was performed utilizing AHe and AFT ages, and associated MTL distributions, with D_{par} (e.g. Donelick et al. 2005) used as a kinetic parameter. Here, we used the QTQt software (version 5.7.0) to determine the thermal history. The QTQt software applies a Bayesian trans-dimensional approach to Markov Chain Monte Carlo statistics (Gallagher 2012) to produce a cooling evolution of the sample that predicts the measured data by applying the AFT annealing model after Ketcham et al. (2007) and the AHe diffusion model after Flowers et al. (2009). In our approach we used an initial unconstrained run to explore the statistical space, that was then followed by adjustments to the search parameters as well as the addition of geological constraints. A large number of iterations ($>>$ 100,000) were run as to generate a range of models that can constrain a probability distribution. From the obtained probability distribution an individual thermal history can be selected, such as the maximum likelihood as well as an "expected" (weighted mean) paths. The general prior was set as t = 26 $\pm$ 1 Ma after a $^{40}Ar/^{39}Ar$ age from a basal tuff in the Cienega basin (Figure 2, Peters et al. 2003) and temperature = 450 $\pm$ 50°C after an assessment of natural mylonitazation temperatures from Stipp et al. (2002). We followed acceptance rates for models were between 0.1 and 0.6 and birth-death ratio was ~1.

4 Results

4.1 Zircon and apatite fission-track

Three samples were collected from a vertical elevation profile along the western-most extent of the Catalina MCC where the high-angle Pirate Fault cross-cuts the Catalina detachment fault (Figure 2 and Table 2). Sample PR-01 (1660 m), PR-02 (1357 m), and PR-03 (1062 m) yielded consistent zircon fission-track ages of 18.8 $\pm$ 1.4 Ma, 19.9 $\pm$ 0.8 Ma, and 19.9 $\pm$ 0.9 Ma, respectively.

Twenty-five samples were selected for apatite fission-track analysis in the Catalina-Rincon MCC (Figure 2 and Table 2) and are presented with published AFT data from Jepson et al. (2021). These samples yielded three subdivisions of apatite fission-track ages; group 1 (two samples) yielded ages $>$ 26 Ma, group-2 (15 samples) yielded ages between ~26 and ~19 Ma, and group-3 (eight samples) yielded ages $<$ ~19 Ma. Group-1 is comprised of samples KJJ09-08 and GM-02. Group-2 is comprised of samples Tort-01, Tort-02, and Tort-03, SP-01, WP-01, LM-02, SC-01, KJJ09-03, KJJ09-07, UoM0422-05, UoM0422-06, UoM0422-10, UoM0422-12, UoM0422-13, UoM0422-15, UoM0422-17, UoM0522-03, and UoM0522-06, and yielded MTLs between 12.9 and 14.1 μm. Group-3 is comprised of samples UoM0422-02, UoM0422-03, UoM0422-04, UoM0422-07, UoM0422-09, UoM0522-02, UoM0522-04, and UoM0522-05, and yielded MTLs of between 13.1 and 14.0 μm. For detailed samples and ages, refer to Table 2 and Supplementary Files 1 and 6.

Table 2: Apatite and zircon fission-track data from the Catalina metamorphic core complex. Samples in italics are from Jepson et al. (2021).

Sample	n[a]	$\rho_s \times$[b] 10^5cm^{-2}	$\rho_D \times$[c] 10^5cm^{-2}	$\rho_i \times$[d] 10^5cm^{-2}	U $\pm 1\sigma$ [e]	D_{par}[f]	χ^2[g]	Age $\pm 1\sigma$[h, i]	MTL (μm) $\pm 1\sigma$ [j]	n[j]
Group 1										
GM-02*	20	1.1	12.3	5.5	5.6 $\pm$ 1.2	2.4	0.91	39.6 $\pm$ 5.7	-	-
KJJ09-08	*20*	*1.1*	*12.1*	*5.2*	*5.4 $\pm$ 0.9*	*2.0*	*0.66*	*40.6 $\pm$ 5.7*	-	-
Group 2										
Tort-01*	20	2.0	13.1	22.7	3.8 $\pm$ 0.3	2.1	0.72	20.0 $\pm$ 1.9	-	-
Tort-02*	20	3.5	12.9	40.0	6.8 $\pm$ 1.0	2.1	0.89	19.0 $\pm$ 1.6	-	-
Tort-03*	20	3.2	12.8	32.0	4.8 $\pm$ 0.7	2.0	0.95	25.0 $\pm$ 2.6	-	-
SP-01*	20	1.4	11.2	11.7	2.3 $\pm$ 0.6	1.8	0.89	23.3 $\pm$ 3.0	-	-

WP-01*	20	1.1	11.1	8.7	1.7 ± 0.1	2.1	1.00	24.3 ± 3.0	-	-
LM-02*	20	1.0	10.9	9.1	1.8 ± 0.3	1.9	0.92	19.8 ± 2.6	-	-
SC-01*	20	1.0	11.4	8.3	1.6 ± 0.2	2.1	1.00	22.2 ± 3.2	-	-
KJJ09-03	*20*	*1.0*	*12.1*	*10.0*	*10.4 ± 1.7*	*2.0*	*0.47*	*21.4 ± 2.6*	-	-
KJJ09-07	*20*	*2.1*	*12.3*	*18.1*	*18.4 ± 2.1*	*2.0*	*0.50*	*24.1 ± 2.2*	*13.7 ± 1.2*	*50*
UoM0422-05	30	0.5	10.3	4.1	5.0 ± 1.0	-	1.00	22.4 ± 2.4	13.1 ± 1.6	11
UoM0422-06	23	3.7	10.4	33.7	40.3 ± 5.2	-	1.00	21.2 ± 1.3	13.7 ± 1.3	42
UoM0422-10	27	2.0	10.9	18.8	21.5 ± 3.5	-	1.00	21.3 ± 1.6	14.1 ± 0.9	64
UoM0422-12	25	1.3	11.1	12.2	13.7 ± 1.3	-	0.79	22.3 ± 1.5	-	-
UoM0422-13	27	1.6	11.2	18.3	18.3 ± 2.1	-	1.00	20.1 ± 1.3	12.9 ± 2.2	54
UoM0422-15	12	1.5	11.7	15.5	16.5 ± 3.2	-	1.00	20.8 ± 2.4	13.8 ± 1.7	32
UoM0422-17	22	2.7	11.9	26.8	28.2 ± 4.6	-	1.00	21.3 ± 1.5	13.7 ± 1.5	101
UoM0522-03	20	0.5	9.3	4.0	5.4 ± 1.4	-	0.06	20.4 ± 1.9	13.3 ± 4.5	5
UoM0522-06	22	1.5	9.9	10.0	12.5 ± 4.2	-	0.00	26.0 ± 7.5	13.6 ± 1.9	6
PR-01 zr	10	37.0	57.5	6.6	565.0 ± 50	-	0.97	18.8 ± 1.4	-	-
PR-02 zr	20	21.0	57.3	3.5	301.0 ± 25	-	1.00	19.9 ± 0.8	-	-
PR-03 zr	15	84.0	57.1	13.9	1205.0 ± 110	-	1.00	19.9 ± 0.9	-	-
Group 3										
UoM0422-02	27	1.6	9.8	19.2	24.4 ± 5.0	-	1.00	15.5 ± 1.3	14.0 ± 1.6	86
UoM0422-03	25	3.6	10.0	42.2	53.1 ± 6.0	-	1.00	15.7 ± 0.9	13.8 ± 1.9	100
UoM0422-04	24	1.6	10.2	18.3	22.5 ± 4.0	-	1.00	16.7 ± 0.9	13.9 ± 1.4	100
UoM0422-07	25	1.0	10.6	13.6	16.0 ± 3.1	-	1.00	14.1 ± 1.2	13.5 ± 2.0	24
UoM0422-09	26	1.3	10.8	14.1	16.4 ± 2.2	-	1.00	17.6 ± 1.3	13.7 ± 1.2	31
UoM0522-02	20	0.7	9.1	6.7	9.0 ± 1.1	-	0.65	18.8 ± 1.9	13.4 ± 3.3	8
UoM0522-04	22	2.1	9.5	22.7	29.9 ± 3.6	-	0.25	17.2 ± 1.2	13.3 ± 1.8	21
UoM0522-05	42	0.8	9.7	9.2	11.9 ± 2.2	-	0.10	15.8 ± 1.9	13.2 ± 1.3	11

[a]number of grains analyzed per sample

[b]density of spontaneous tracks counted

[c]density of dosimeter tracks counted

[d]density of induced tracks counted

[e]average concentration of ^{238}uranium

[f]average length of the etch pits in μm

[g]probability that single grain ages belong to the same population

[h]central age (Ma) for apatite fission-track using ζ-value of 341.6 (8.5, GJ with asterisk) and 368.0 (13.0, TC)

[i]central age (Ma) for zircon fission-track using ζ-value of 116.0 (1.3, SNT with zr)

[j]mean track length and number of confined fission-tracks

234

235 Zircon and apatite (U-Th-[Sm])/He

236 Four samples were selected for ZHe analysis in the Catalina-Rincon MCC (Figure 2 and Table 3). Sam-
237 ples LM-02, SC-01, WP-01, and SP-01 yielded ZHe ages of 20.8 $\pm$ 0.4 Ma, 22.3 $\pm$ 0.5 Ma, 25.8 $\pm$ 0.8,
238 and 24.0 $\pm$ 0.5 Ma, respectively.

239 Twenty-three samples were selected for AHe analysis in the Catalina-Rincon MCC (Figure 2 and
240 Table 3). Using the same subdivisions for AHe ages as outlined in the apatite fission-track results; group
241 1 (no samples) yielded ages $>$ 26 Ma, group-2 (nine samples) yielded ages between 26 and 19 Ma, and
242 group-3 (15 samples) yielded ages $<$ 19 Ma. Group-2 comprises of samples WP-01, SP-01, UoM0422-
243 09, UoM0422-10, UoM0422-12, UoM0522-01, UoM0522-02, UoM0522-05, and UoM0522-06. Group-3
244 comprises samples LM-02, SC-01, UoM0422-02, UoM0422-03, UoM0422-04, UoM0422-05, UoM0422-
245 06, UoM0422-07, UoM0422-09, UoM0422-13, UoM0422-14, UoM0422-15, UoM0422-17, UoM0522-03,
246 and UoM0522-04). A number of factors have been invoked to explain single grain AHe age dispersion
247 such as radiation damage, spherical equivalent grain radius, grain fragmentation, U-Th zonation, U- and
248 Th-bearing inclusions, He implantation, chemical composition and crystal imperfections (e.g. Shuster
249 et al. 2006, Fitzgerald et al. 2006, Brown et al. 2013, Wildman et al. 2016, Gerin et al. 2017, Zeitler et al.
250 2017) . However, many of our analyses were obtained via multiple grain dissolution (denoted by #, Table
251 3, e.g. Spiegel et al. 2009). Thus, spurious ages may stem from averaging across multiple grains. For
252 detailed samples and ages the reader is referred to Table 3 and Supplementary File 3.

Table 3: Apatite and zircon (U-Th-[Sm])/He data from the Catalina metamorphic core complex. Text in bold is the weighted mean age ± 2 standard error. Samples in italics were excluded from age calculation. Standard data and unique lab ID for each sample can be found in Supplementary File 3.

Sample	#[a]	U (ppm)	Th (ppm)	Sm (ppm)	eU[b]	F_T[c]	^{4}He (ncc)	Mass (mg)	Raw Age	Corr. Age ± 1σ	MWAR (μ)[d]	SD[e]
Group 2												
WP-01	1	7.8	1.7	274.2	8.2	0.834	0.330	16.3	19.7	23.7 ± 0.5	93.0	-
	1	9.0	1.9	315.0	9.5	0.883	0.876	34.9	21.0	23.8 ± 0.4	114.0	-
											23.8 ± 0.6 Ma	
SP-01	1	6.9	6.6	280.5	3.8	0.729	0.063	2.8	21.0	28.8 ± 1.7	51.0	-
	1	3.2	2.2	255.7	7.7	0.804	0.056	6.7	17.2	21.4 ± 1.5	68.5	-
											24.6 ± 2.2 Ma	
UoM0422-09	1	13.7	1.7	438.6	14.1	0.89	1.002	0.0261	21.5	24.2 ± 3.0	[f]224.9	[g]330.7
	2	4.0	1.6	81.5	4.4	0.76	0.068	0.0094	13.3	17.5 ± 2.2	63.5	6.2
	4	2.9	3.0	110	3.6	0.82	0.608	0.0629	21.0	25.5 ± 1.6	79.6	8.4
	2	-	-	-	*1.27*	*1.00*	*0.424*	-	*40.0*	*40.0 ± 2.5*	-	-
	3	-	-	-	0.52	1.00	0.560	-	23.1	23.1 ± 1.4	-	-
											23.0 ± 1.8 Ma	
UoM0422-10	4	5.1	11.4	30.8	7.8	0.73	0.323	0.0209	16.2	22.1 ± 2.7	54.9	2.6
	5	8.0	13.1	25.9	11.1	0.70	0.327	0.0149	16.2	23.3 ± 2.9	43.9	4.8
	2	-	-	-	2.99	1.00	1.331	-	18.4	18.4 ± 1.1	-	-
	4	-	-	-	1.90	1.00	0.978	-	20.7	20.7 ± 1.3	-	-
											19.9 ± 1.6 Ma	
UoM0522-06	5	6.4	2.5	89.8	7.0	0.75	0.381	0.0255	17.4	23.1 ± 1.4	61.5	18.9
											23.1 ± 2.8 Ma	
UoM0422-12	7	3.6	7.4	245.0	5.3	0.69	0.223	0.0204	15.8	22.8 ± 2.8	47.0	5.2
	6	2.7	4.6	191.2	3.8	0.70	0.151	0.0156	19.8	28.1 ± 3.5	52.2	9.1
	1	-	-	-	1.39	1.00	0.905	-	27.3	27.3 ± 1.7	-	-
	2	-	-	-	0.50	1.00	2.380	-	25.9	25.9 ± 1.6	-	-
											26.2 ± 2.0 Ma	
UoM0522-01	1	7.6	4.4	225.6	8.6	0.81	0.193	0.0105	17.0	21.0 ± 1.3	[f]170.5	[g]156.8

	1	6.2	5.0	247.1	7.4	0.85	0.368	0.0234	16.7	19.7 ± 1.2	[f]250.5	[g]192.8
	1	*3.2*	*3.2*	*79.4*	*4.0*	*0.82*	*0.148*	*0.0135*	*22.3*	*27.2 ± 1.7*	*[f]195.9*	*[g]165.8*
	1	19.8	9.4	457.8	22.0	0.82	0.362	0.0087	15.1	18.4 ± 1.1	[f]204.9	[g]167.8
											20.6 ± 1.2 Ma	
UoM0522-02	4	6.4	3.5	104.1	7.2	0.81	0.790	0.0396	22.2	27.3 ± 1.7	73.2	11.2
	4	*7.7*	*11.7*	*109.8*	*10.5*	*0.79*	*0.393*	*0.0295*	*10.4*	*13.0 ± 0.8*	*56.8*	*22.8*
	5	8.8	3.2	164.1	10.0	0.76	0.553	0.0248	18.8	24.7 ± 1.5	56.4	5.4
											25.8 ± 2.2 Ma	
UoM0522-05	5	5.5	21.4	170.1	10.5	0.69	0.332	0.0127	19.9	28.9 ± 1.8	47.8	6.8
	5	*4.9*	*10.1*	*88.1*	*7.3*	*0.70*	*0.121*	*0.0147*	*9.2*	*13.1 ± 0.8*	*49.2*	*5.8*
	5	12.8	30.7	233.9	20.0	0.63	0.221	0.0074	12.2	19.1 ± 1.2	37.7	6.9
											22.1 ± 2.0 Ma	
LM-02 zr[h]	1	454.9	106.4	-	479.9	0.77	6.4	6.9	20.0	20.8 ± 0.4	-	-
											20.8 ± 0.4 Ma	
SC-01 zr	1	782.7	213.0	-	832.8	0.78	20.5	11.7	17.3	22.3 ± 0.5	-	-
											22.3 ± 0.5 Ma	
WP-01 zr	1	301.2	141.1	-	334.4	0.84	18.9	21.5	21.7	25.8 ± 0.8	-	-
											25.8 ± 0.8 Ma	
SP-01 zr	1	4627.6	434.6	-	4729.7	0.81	101.9	9.1	20.6	24.0 ± 0.5	-	-
											24.0 ± 0.5 Ma	
Group 3												
LM-02	1	6.2	2.6	57.0	6.9	0.827	0.081	10.4	9.4	11.3 ± 0.6	76.5	-
	1	3.6	0.9	28.8	3.8	0.823	0.060	14.0	9.3	11.3 ± 0.8	73.0	-
											11.3 ± 1.0 Ma	
SC-01	1	8.1	3.8	83.8	9.0	0.744	0.061	4.7	11.7	15.8 ± 1.0	54.0	-
	1	2.0	0.7	77.3	2.2	0.887	0.076	32.4	8.6	9.7 ± 0.5	126.0	-
											10.9 ± 1.0 Ma	
UoM0422-02	7	16.3	7.8	36.2	18.1	0.70	0.438	0.0220	9.0	12.9 ± 1.6	47.4	5.0
	6	10.0	4.0	25.3	10.9	0.69	0.206	0.0160	9.7	14.0 ± 1.7	50.4	8.8
	9	*8.2*	*4.6*	*18.3*	*9.3*	*0.73*	*0.727*	*0.321*	*19.9*	*27.5 ± 3.4*	*54.0*	*4.8*
	4	13.5	8.0	34.5	15.4	0.84	1.533	0.0830	9.8	11.7 ± 0.7	92.3	18.1

	4	12.2	6.1	25.9	13.6	0.88	2.626	0.1570	10.1	11.5 ± 0.7	108.5	16.3
	4	10.1	5.1	24.8	11.3	0.82	0.921	0.0522	12.8	15.6 ± 1.0	79.1	12.2
											12.6 ± 0.8 Ma	
UoM0422-03	8	32.8	13.2	52.9	35.9	0.73	1.575	0.0300	12.0	16.4 ± 2.0	52.2	4.5
	5	35.3	15.3	54.5	38.9	0.76	1.110	0.0246	9.5	12.6 ± 1.6	57.1	6.8
	5	27.5	12.6	51.3	30.5	0.80	1.835	0.0450	10.9	13.7 ± 1.7	66.6	9.6
	8	*0.7*	*0.2*	*1.7*	*0.8*	*0.8*	*2.100*	*0.0386*	*547.0*	*726.6 ± 90.1*	*58.8*	*9.7*
											14.0 ± 2.0 Ma	
UoM0422-04	5	18.7	48.1	55.8	30.0	0.74	0.714	0.0205	9.5	12.9 ± 1.6	56.8	2.3
	7	14.8	43.2	53.9	25.0	0.68	0.406	0.0164	8.1	11.9 ± 1.5	47.8	2.2
	4	7.8	25.5	47.0	13.8	0.83	1.404	0.8210	10.2	12.2 ± 0.8	79.2	14.9
											12.3 ± 1.4 Ma	
UoM0422-05	6	3.4	1.1	64.0	3.7	0.74	0.124	0.0270	10.1	13.6 ± 1.7	56.2	4.6
	4	3.1	0.9	66.4	3.3	0.80	0.173	0.0375	11.2	14.0 ± 1.7	72.6	7.5
											13.8 ± 2.4 Ma	
UoM0422-06	6	18.1	2.8	2.6	18.8	0.72	0.563	0.0204	12.1	16.7 ± 2.1	54.3	5.0
	5	21.0	4.4	2.8	22.0	0.73	0.571	0.0017	12.3	16.7 ± 2.1	54.6	8.8
	6	*12.4*	*3.8*	*5.7*	*13.3*	*0.71*	*0.486*	*0.0152*	*19.8*	*27.9 ± 3.5*	*43.8*	*3.5*
	4	17.1	3.7	4.9	18.0	0.84	2.208	0.0756	13.4	16.0 ± 1.0	79.7	14.1
	4	19.0	5.1	6.5	20.2	0.84	1.851	0.0754	10.0	12.0 ± 0.7	74.3	8.5
											13.8 ± 1.0 Ma	
UoM0422-07	6	4.3	3.7	40.0	5.2	0.79	0.306	0.0455	10.7	13.6 ± 1.7	73.3	6.8
	7	5.2	3.9	37.4	6.1	0.74	0.278	0.0341	10.9	14.7 ± 1.8	57.2	4.4
											14.1 ± 2.4 Ma	
UoM0422-13	3	7.5	1.8	178.4	7.9	0.85	0.708	0.0568	12.5	14.8 ± 1.8	98.2	9.4
	4	9.2	1.9	121.4	9.7	0.75	0.262	0.0179	12.3	16.3 ± 2.0	61.9	2.8
	4	6.2	1.8	225.7	6.6	0.70	0.089	0.0113	9.4	13.4 ± 1.7	59.7	3.3
	4	*6.2*	*2.9*	*150.9*	*6.9*	*0.83*	*1.129*	*0.0589*	*22.2*	*26.6 ± 1.7*	*77.1*	*16.4*
	4	4.1	2.0	113.1	4.6	0.82	0.458	0.0613	13.2	16.0 ± 1.0	72.3	14.5

											15.4 ± 3.2 Ma
UoM0422-14	5	8.9	5.0	131.5	10.1	0.69	0.141	0.0121	9.4	13.7 ± 1.7	48.2	2.4
	4	*1.2*	*1.0*	*110.1*	*1.4*	*0.70*	*0.101*	*0.0104*	*51.4*	*73.3 ± 9.1*	*54.4*	*4.3*
	2	16.1	19.1	130.7	20.6	0.74	0.111	0.0075	5.8	7.9 ± 1.0	52.6	21.7
											9.4 ± 1.8 Ma
UoM0422-15	5	6.5	15.1	45.3	10.1	0.70	0.173	0.0126	11.2	15.9 ± 2.0	50.1	6.0
	4	10.3	24.1	71.5	16.0	0.71	0.253	0.0114	11.4	16.0 ± 2.0	55.4	8.7
	4	6.3	16	36.3	10.1	0.81	0.647	0.0476	11.0	13.6 ± 0.8	75.1	12.6
	4	7.7	16.1	43.0	11.5	0.78	0.428	0.0326	9.3	11.9 ± 0.7	65.8	4.5
											13.0 ± 1.0 Ma
UoM0422-17	5	13.1	0.7	178.2	13.3	0.80	0.714	0.0390	11.2	14.0 ± 1.7	61.4	7.4
	4	18.0	0.9	227.6	18.2	0.77	0.565	0.0232	10.8	14.1 ± 1.8	62.8	5.0
	5	*18.9*	*1.4*	*201.5*	*19.2*	*0.74*	*0.108*	*0.0202*	*2.3*	*3.1 ± 0.4*	*55.7*	*4.8*
											14.1 ± 2.4 Ma
UoM0522-03	3	2.7	2.9	69.9	3.4	0.86	0.592	0.0861	16.5	19.2 ± 1.2	95.3	14.9
	5	2.6	2.3	49.1	3.1	0.84	0.349	0.0825	10.8	12.8 ± 0.8	85.7	14.8
	5	2.3	1.6	54.7	2.7	0.82	0.355	0.0697	15.3	18.6 ± 1.2	91.0	27.7
											15.7 ± 1.2 Ma
UoM0522-04	5	9.0	2.1	38.9	9.5	0.79	0.586	0.0378	13.4	16.9 ± 1.0	66.5	14.7
	5	1.8	1.2	9.6	2.1	0.72	0.041	0.0177	9.2	12.7 ± 0.8	49.2	5.4
											14.3 ± 1.2 Ma

[a]number of single grains used in bulk degassing (Spiegel et al. 2009)

[b]effective uranium scaled for relative alpha production rate ($U(ppm) + 0.235 \times Th(ppm)$)

[c]alpha-ejection correction after (Farley 2002)

[d]mass weighted average radius of apatite crystals measured in the aliquot analyzed

[e]Standard deviation of the MWAR is used as a guide for the 'tightness of the range of single crystal radii picked within a sample.

[f], [g]Single grain length and width are indicated by [f] and [g], respectively

[g], samples denoted with "zr" are zircon.

253

4.2 Crustal thickness estimates

Crustal thickness estimates from compiled whole rock data range from 72 to 18 km. An individual crustal thickness estimate can have uncertainties as high as 10 km (e.g. Chapman et al. 2015, 2020). Thus, to improve the resolution, crustal thickness estimates were binned into 10 Ma intervals, with a median crustal thickness calculated for each interval. The 10 myr intervals were selected through an iterative process to balance reasonable estimates on the crustal thickness at a given time period with resolution of documented thinning episodes. Intervals 70-60 Ma, 60-50 Ma, 50-40 Ma, 40-30 Ma, 30-20 Ma, and 20-10 Ma yielded a weighted mean crustal thickness estimate and associated error was calculated (assuming $\pm$ 10 km uncertainty for an individual estimate) of 59.6 $\pm$ 2.7 km, 51.8 $\pm$ 3.0 km, 36.3 $\pm$ 5.0 km, 44.0 $\pm$ 2.0 km, 45.1 $\pm$ 2.4 km and 35.9 $\pm$ 5.0 km, respectively. These data show elevated crustal thicknesses estimates of ~60 km at 70-60 Ma decreasing to crustal thickness estimates of ~45-40 km between 40 and 20 Ma, before a slight decrease in crustal thicknesses to ~38 km at 20-10 Ma. Considering the paucity and scatter of data-points at 50-40 Ma interval, we exclude this interval from further interpretation. In summary, these data identify two distinct phases of crustal thinning; 1) a sharp decrease in crustal thickness estimates between 70 and 40 Ma, and 2) a more modest period of thinning between ~30-20 Ma and ~20-10 Ma (Figure 3).

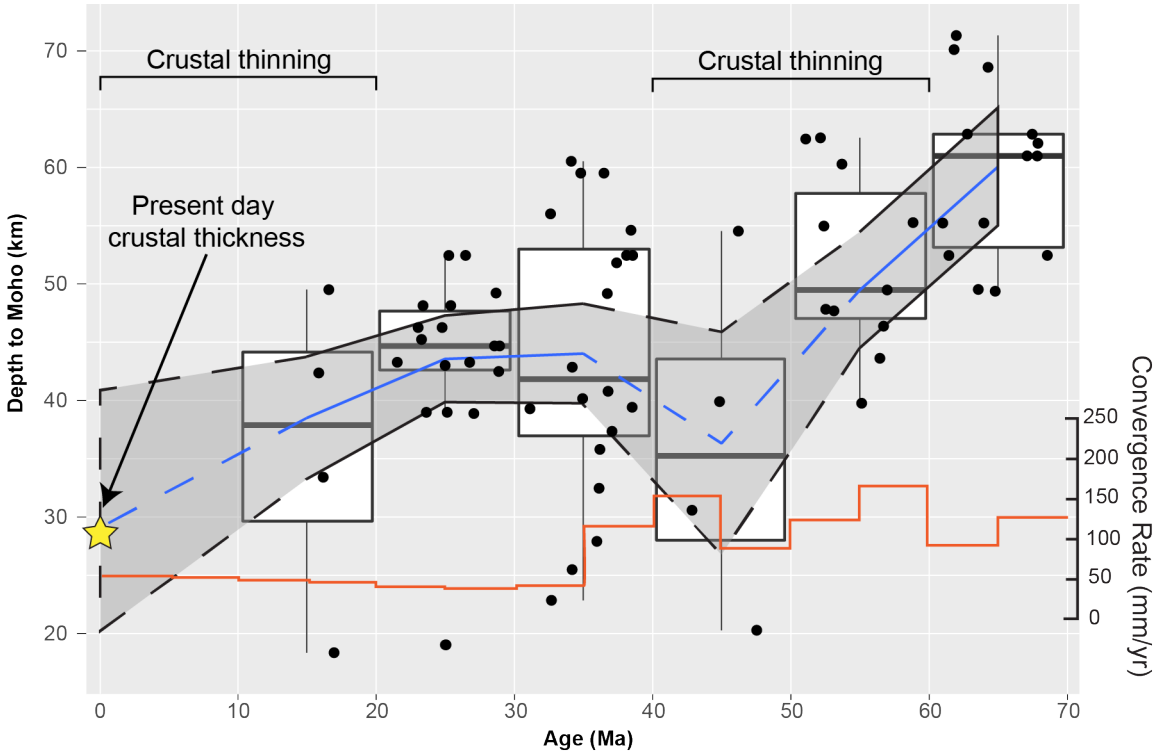

Figure 3: Sr/Y crustal thickness estimates from southern Arizona, eastern California, and western New Mexico through time. Box plots give the median crustal thickness estimate for each 10 myr interval and whiskers illustrate minimum and maximum constraints. Depth to Moho is analogous to crustal thickness. Blue line and grey envelope is mean spline and 1-standard error limit. Dashed line illustrates paucity of data constraining the 50-40 Ma time interval. Orange line is the convergence velocity between the Farallon and North American plates in mm per year from (Seton et al. 2012). Detailed sample information can be found in Supplementary File 4. Data points within each 10 myr bin have been separated to visualize crustal thickness estimate variation.

4.3 Thermal History Modelling

Four representative samples (UoM0422-12, WP-01, KJJ09-03, and UoM0422-06), were selected together as an elevation profile (2291 m, 2004 m, 1608 m, and 1085 m, respectively) for thermal history modelling (Figure 2, e.g. Gallagher et al. 2005). These four samples comprise a vertical transect within lower-plate rocks from the base of the Catalina MCC to near its highest elevation at this locality. Samples which yielded Eocene cooling ages did not have sufficient confined track lengths for thermal history modelling. Confined track distributions, individual models, and modelling parameters are available in Table 2 and 3, and Supplementary File 5. The AFT data for sample KJJ09-03 from Jepson et al. (2021) was combined with AHe data from sample UoM0522-01 from this study as they were collected from the same locality. The thermal history model indicates two periods of cooling following onset of detachment at ~26 Ma (Peters et al. 2003). Initially, the elevation profile (samples UoM0422-12, WP-01, KJJ09-03, and

UoM0422-06) undergoes rapid cooling from ~450 $\pm$ 50 °C at 26 Ma to ~80 °C at 21 Ma at a rate of ~74 °C per myr. After this phase of rapid cooling, the samples then transition to a period of more protracted cooling from ~80 °C at ~21 Ma to $\leq$ 40 °C at ~9 Ma at a rate of ~4 °C per myr (Figure 4). As part of the model formulation using an elevation profile, it is possible to obtain an estimate of the paleo-geothermal temperature gradient through time (Gallagher et al. 2005, Gallagher 2012). This is based, in part, on the assumption that the samples remain in constant vertical offset and thus temperature offset through time (Gallagher et al. 2005). From our thermal history model we obtain a paleo-geothermal gradient of ~45 $\pm$ 6 °C per km from 26 to 19 Ma, and a paleo-geothermal gradient of ~41-29$\pm$ 5 °C per km from 19 to 11 Ma (Figure 4).

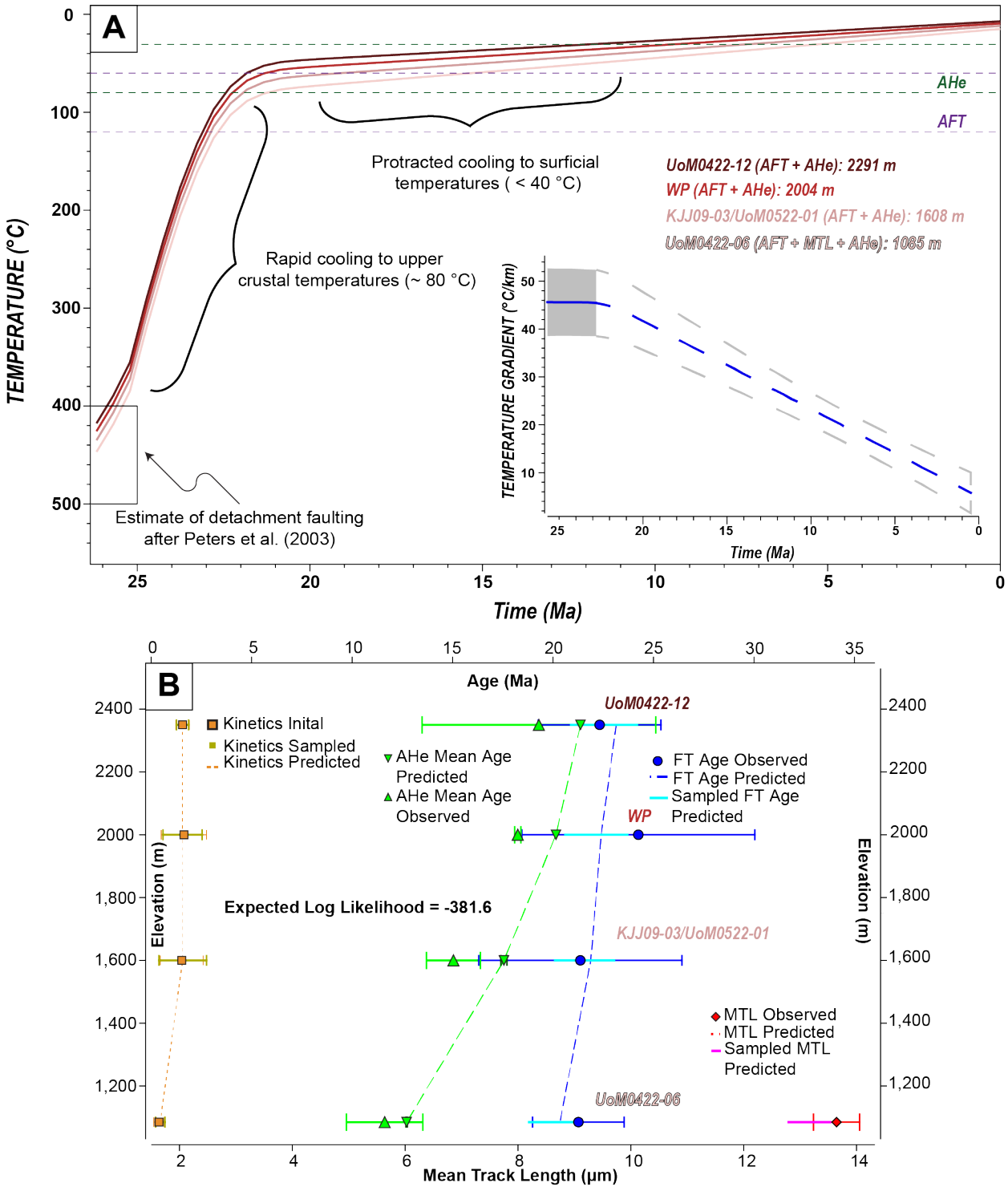

Figure 4: A) Representative thermal history model and paleo-geothermal gradient of the Catalina Metamorphic Core Complex indicating rapid cooling from temperatures of ~500-450 °C (e.g. Stipp et al. 2002) following the best estimate for the onset of detachment faulting (Peters et al. 2003) and transitioning to relatively slower cooling during the Basin and Range. Green and purple dashed lines indicate the apatite partial retention zone and partial annealing zone, respectively (e.g. Braun et al. 2006). Samples used were from an elevation profile indicated in Figure 2, using apatite fission-track (AFT), apatite (U-Th-Sm)/He (AHe), and mean track length (MTL) data from this study and Jepson et al. (2021). Uncertainty on the paleo-geothermal estimate is indicated by the grey shading. Paleo-geothermal gradient decreases towards present day indicated by dashed line and outline at atmospheric temperature lapse rate of ~5-6 °C/km (Gallagher et al. 2005) and is unlikely to be an accurate estimate of the geothermal gradient. Modelling was performed using QTQt 5.7.0 (Gallagher 2012). B) Observed versus predicted values for all data used in the thermal history model. FT is fission-track and MTL is mean track length.

5 Discussion

Here, we detail a polyphase Cenozoic cooling and exhumational history of the Catalina-Rincon MCC in southern Arizona. Integrated with previously published data from the Catalina MCC, AHe (n = 34), AFT (n = 31), ZHe, (n = 4), and ZFT (n = 17), our study constrains three main periods of cooling: 1) an early phase of cooling prior to ~40 Ma (Figure 5); 2) a major phase of cooling between 26 and 19 Ma; and 3) a late period of cooling occurring between 17 and 11 Ma (Figure 5, this study, Fayon et al. 2000, Jepson et al. 2021). The three cooling phases were determined by integrating the thermal history modelling (Figure 4) with the total distribution of low-temperature cooling ages across the Catalina MCC (Figure 5). We compare the interpreted cooling phases with crustal thickness estimates for southern Arizona (Figure 3) to resolve the tectonic processes behind thinning of the hypothesized Arizona-plano crust. To convert cooling ages to crustal depth a geothermal gradient is required (e.g. Braun et al. 2006). In the following discussion we use a paleo-geothermal gradient based on our thermal history modelling of 45 °C/km from 26 to 19 Ma and a paleo-geothermal gradient of ~25 °C/km from 19 to 11 Ma (Figure 4). For the Eocene-Oligocene, this is in agreement with paleo-geothermal gradients which have been suggested in southern Arizona (40-50 °C/km, Ducea et al. 2020, and references therein). The modelled Miocene paleo-geothermal gradient is likely not reflective of crustal thermal conditions, as the samples have already cooled to the upper-crust by this time and provide no additional constraints (Gallagher et al. 2005). Therefore, we select a relatively standard geothermal gradient of 25 °C/km after heat flow modelling in Ketcham (1996). Despite the uncertainty, these estimates provide robust maximum depth constraints for comparison between different tectonic events.

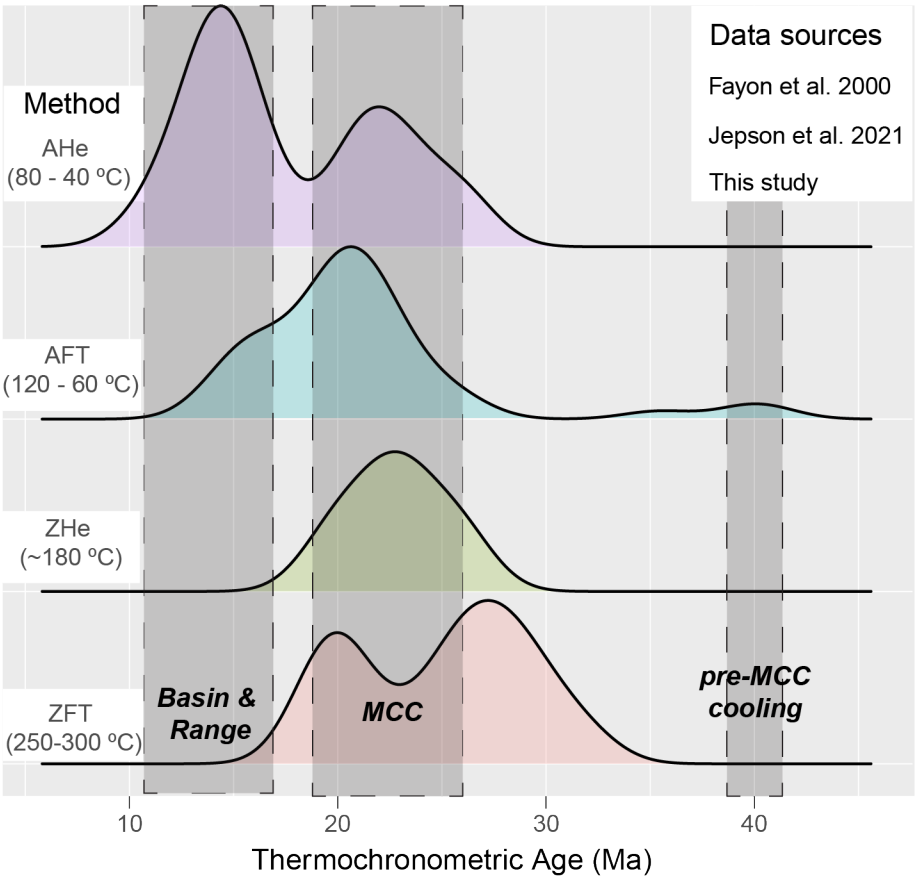

Figure 5: Kernel density estimates of combined zircon and apatite fission-track (ZFT, AFT) and zircon and apatite (U-Th-Sm)/He (ZHe and AHe) from this study, Fayon et al. (2000) and Jepson et al. (2021). The combined thermochronometers (temperatures from Braun et al. (2006)) constrain two major periods of cooling associated with the Basin and Range (11-17 Ma) and Metamorphic Core Complex (MCC, 19-26 Ma) events, and a minor, pre-MCC phase at *ca.* 40 Ma. Data-points are separated along the y-axis for visualization.

Pre-metamorphic core complex exhumation (~40 Ma): Middle- to lower-crustal processes?

In this study, we note *ca.* 40 Ma AFT ages on the eastern flank of the Catalina MCC and the western margin of the Galiauro Mountains (Figure 2, Jepson et al. 2021). This is anomalous, as the bulk of the thermochronometric data from the Catalina MCC records cooling that is $\leq$ 26 Ma (Figure 6, see also; Creasey et al. 1976, Fayon et al. 2000, Jepson et al. 2021). Given the occurrence of Eocene AFT ages on the NE side of the Catalina MCC, spatially disparate localities, and absence of confined fission-track lengths, we consider these samples as structurally closer to the Eocene paleo-surface and thus, were likely residing in the apatite PAZ. Therefore, these ~40 Ma cooling ages likely represent mixed ages between an older $\geq$ 26 Ma pre-MCC cooling event and the younger $\leq$ 26 Ma MCC cooling event (e.g. Wildman et al. 2016). However, these cooling ages are notably consistent with other studies in southern

Arizona which have observed upper-crustal cooling at this time (Riley 2004, Caylor et al. 2021), which suggests that this episode of minor cooling was regionally widespread.

In southern Arizona, the crustal thickness estimates show a period of thinning of ~10 km, from thicknesses of ~50 km at 60-50 Ma to thicknesses of ~40 km at 40-30 Ma (Figure 7). No upper-crustal extension has been recognized during this time interval. Further, the resolution of the Eocene upper-crustal cooling period is also poor, as they resolve a mixed age between the pre-MCC and MCC events. However, pre-MCC thermochronometric cooling ages are observed in Walker Lane, Nevada (Say & Zuza 2021) and higher temperature cooling has been documented within the Catalina MCC (Ducea et al. 2020, Jepson et al. 2021), suggesting that this pre-MCC cooling may be more widespread than previously considered (Singleton et al. 2018). Despite the opaqueness surrounding this pre-MCC tectonic event, the presence of mixed thermochronometric ages and the lack of normal faulting structures, discussed below, cannot explain the ~10 km record of crustal thinning based on regional crustal thickness estimates (Figure 3). Thus, an additional mechanism is required to thin the thickened Laramide crust prior to the onset of MCC detachment faulting.

There are several factors that could explain the discrepancy between the cryptic upper-crustal cooling and a rapid period of crustal thinning. Firstly, the older, mixed thermochronometric ages may represent thermal relaxation following Paleogene intrusions (Terrien 2012, Fornash et al. 2013). However, this would likely correspond to either stability or thickening in crustal thickness estimates, not thinning which is observed (Figure 3). Secondly, the cooling could be explained by extension or late-stage Laramide thrust faulting. Laramide tectonic activity which has been dated to *ca.* 76-50 Ma within southern Arizona and western New Mexico (e.g. Copeland et al. 2017), which could provide a mechanism for a pre-MCC cooling. However, reverse faulting and thrusting thicken the crust, inconsistent with the thinning observed and Paleocene-Eocene upper-crustal extensional structures are absent across southern Arizona (Davis et al. 2004). Further, although Farallon slab roll-back initiated in the Paleocene-Eocene (e.g. Saleeby 2003), the Farallon slab was still in-place under southern Arizona-New Mexico by the middle-Eocene (Coney & Reynolds 1977, Copeland et al. 2017, Bahadori et al. 2018), likely preventing whole-scale extension. An alternative lower-crustal mechanism could be the localized foundering of an eclogitic crustal root, which generated crustal thinning and upper-crustal uplift (e.g. DeCelles et al. 2009). However, this hypothesis may be hindered by the presence of the Farallon slab at this time.

Ductile flow of the middle- to lower-crust can thin the crust and generate limited upper-crustal cool-

ing without major upper-crustal extension (Figure 7, Lavier & Manatschal 2006). Lateral extrusion of the lower-crust is hypothesized to occur beneath high plateaus, in which the hot, weak lower-crust is evacuated, smoothing the topography (Bird 1991), particularly near extensional MCCs (McKenzie & Jackson 2002). In modern day thickened crusts of Tibet and the Altiplano, lower-crustal flow has been inferred, moving material from thickened plateau interiors toward the thinner margins and cooling the crust (e.g. Royden et al. 1997, Gerbault et al. 2005, Enkelmann et al. 2006). Lower-crustal flow has also been proposed for the Laramide, which decoupled lower-crustal and upper-mantle traction (Royden et al. 1997, Hyndman 2017, Schutt et al. 2018). Further, the convergence velocity of the Farallon plate is modelled to have slowed sharply during the Eocene (e.g. Seton et al. 2012, Yonkee & Weil 2015, Wright et al. 2016), which could have diminished the compressive stress acting on Laramide crust and allowed for ductile middle- to lower-crustal processes to thin the crust (Figure 7). Eocene ductile middle- to lower-crustal processes are supported by observations by Ducea et al. (2020) who suggested that much of the ductile fabric in the Catalina MCC formed during the Eocene based on the dating of syn-kinematic felsic dikes. Further, ϵHf and ϵNd signatures from the 57-45 Ma Wilderness Suite suggest that melts crystallized at this time were relatively evolved (Fornash et al. 2013) supporting the hypothesis of a hot, melt rich crust, conditions favorable to lower-crustal flow. Finally, we suggest that ductile crust likely flowed either to the south or south-west, as the Colorado Plateau remains to the north (Figure 7). It is likely that the ~40 Ma cooling event was regionally more widespread, however subsequent erosion would have removed more extensive evidence leaving a fragmented basement record. The basin record of this Eocene cooling would be stored in proximal basins.

Metamorphic core complex exhumation (26-19 Ma): Detachment faulting

The modern morphology of the Catalina MCC is reflective of the SW dipping low-angle detachment-fault system (e.g. Davis & Coney 1979, Davis 1987). The earliest onset of detachment faulting is at *ca.* 26 Ma (Peters et al. 2003), which rapidly exposed the deformed ductile middle-crust (~10-15 km) to the surface (Lister & Davis 1989). This process of crystal plastic deformation, detachment faulting and subsequent exhumation is traditionally thought to have generated much of the widespread mylonitic fabric exposed throughout the Catalina MCC (Davis 2013, Spencer et al. 2019, and references therein). Fayon et al. (2000) identify early Oligocene cooling through ZFT thermochronology and suggest extension as initiating at ~30 Ma. However, these data may also reflect a mixed age between pre-MCC and MCC cooling events as discussed above. Peters et al. (2003) constrained detachment to be active at ~26

Ma consistent with all thermochronometric data presented in this study, which suggests detachment was ongoing at this time. As a result of the extensive and rapid exhumation, the majority of cooling ages (~60%) identified through low-temperature thermochronology in this and previous studies are Oligocene-Miocene (Creasey et al. 1976, Fayon et al. 2000, Jepson et al. 2021). Given the presence of ductile strain mechanisms in quartz and brittle strain mechanisms in feldspar within the mylonitic fabric, workers have assessed that the mylonitic fabric formed at ~500-300 °C (e.g. Stipp et al. 2002). Therefore, given the abundance of low-temperature thermochronometric ages between *ca.* 26 and 19 Ma coupled with cooling estimates from the thermal history model, we infer that the Catalina MCC cooled from ~500-450 °C to ~80 °C rapidly during the late Oligocene-early Miocene (within ~1 to 7 myr, Figure 4). The Catalina MCC displays a clear trend of younger thermochronometric ages with lower elevation indicating a rapid apparent exhumation rate from *ca.* 26-19 Ma (apparent exhumation rate of 0.24 mm/yr, Figure 6).

The onset of detachment faulting and subsequent MCC exhumation has been identified as a major contributor to thinning of previously thickened crust (e.g. Lister & Davis 1989). In southern Arizona, the crustal thickness record demonstrates thinning from crustal thicknesses of ~45 km at 30-20 Ma to ~37 km at 20-10 Ma (Figure 3). This followed a period of relative stability from 40-30 Ma to 30-20 Ma, where crustal thickness was ~45.1 $\pm$ 2.4 km. Based on rapid cooling from 450 °C to ~80 °C (Figure 4) and a paleo-geothermal gradient of ~45 °C/km, we assess an upper limit of ~8 km of material denuded from the Catalina MCC (Figure 5), within uncertainty of the ~8 km identified via crustal thickness estimates (Figure 3). Therefore, we suggest that at least twice as much crustal material was removed from the Catalina MCC during detachment faulting in comparison with Basin and Range extension (Figure 6).

Regionally, the occurrence of rapid Oligocene-Miocene exhumation from the brittle-to-ductile transition to the uppermost crust has been observed in both the Pinaleño (*ca.* 31 to 25 Ma) and Coyote Mountains MCCs (*ca.* 29 to 21 Ma; Long et al. 1995, Gottardi et al. 2020, Jepson et al. 2021) which are situated to the NE and SW of the Catalina MCC, respectively. Farther afield, the California-Arizona MCCs such as the Buckskin-Rawhide and Whipple Mountain MCCs demonstrate a similar magnitude of Oligocene-Miocene exhumation, with initiation occurring more recently at *ca.* 24 Ma (e.g. Davis 1988, Lister & Davis 1989, Foster et al. 1993). Mylonitization associated with the Sonoran Anochi and Magdalena-Madea MCCs to the south also occurred slightly earlier (~34-25 Ma Wong & Gans 2008, Gottardi et al. 2020, and references therein). The hypothesized timing of California-Arizona-Sonora MCC extension (*ca.* 26-21 Ma) is coeval with the timing of slip along the Orocopia Mountains Detachment Fault in southwestern California (Jacobson et al. 2007, Moser et al. 2021). The synchronous timing of rapid cooling throughout

southwestern US and northern Mexico underscores the large-scale, regional attenuation of the crust at this time (Coney 1980, Davis & Hardy Jr. 1981, Whitney et al. 2013, Platt et al. 2015).

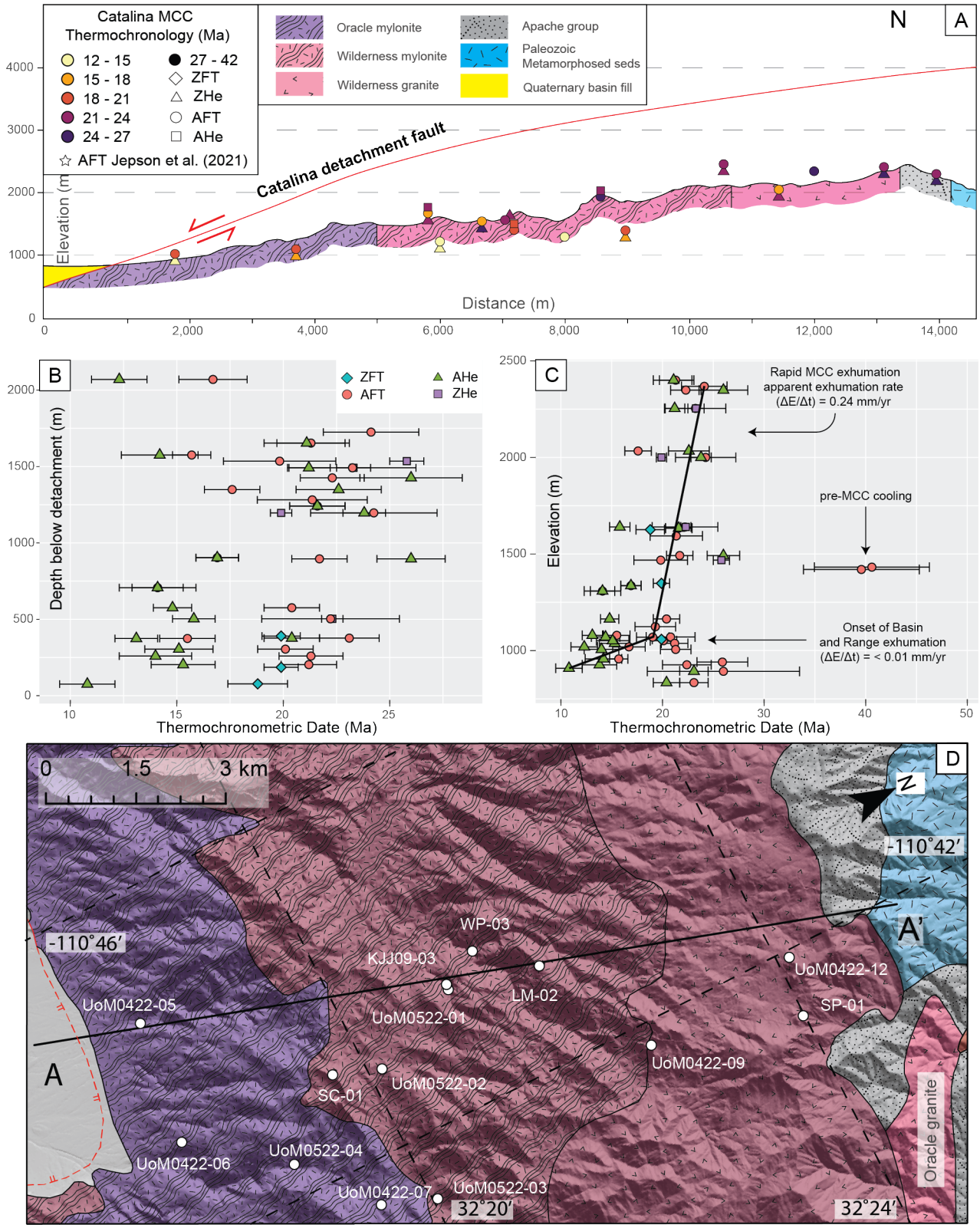

Figure 6: Caption continued on next page.

Figure 6: A) Cross-section of the Catalina Metamorphic Core Complex (MCC) indicating thermchronometric age versus elevation, with the projected Catalina detachment fault, ZFT = zircon fission-track, AFT = apatite fission-track, ZHe = zircon (U-Th)/He, and AHe = apatite (U-Th-Sm)/He. Cross-section shows no vertical exaggeration. Units are colored following Arca & Johnson (2010, and references therein). B) Plot displaying thermochronometric age against depth below the detachment. Depth to detachment was calculated by closest distance between sample locations and a 3D interpolation of the detachment surface constrained by surface exposure of the corrugated detachment surface. C) Plot displaying thermochronometric age against elevation. Break-in-slope at ~19 Ma identifies transition between rapid apparent exhumation (change in elevation/change in age) during MCC detachment faulting to slower exhumation during Basin and Range faulting. D) Geological map of the cross-sectioned area after Arca & Johnson (2010) showing locations of samples.

Basin and Range exhumation (17-11 Ma): High-angle normal faulting

The most recent phase of exhumation was in response to high-angle normal-faulting related to Basin and Range extension (e.g. Dickinson 1991, Singleton et al. 2019). Within the Catalina MCC the Basin and Range extension is manifested by brittle NE-SW striking faults (the Pirate Fault, Figure 2 Davis et al. 2004). Although structures related to E-W Basin and Range extension are prevalent throughout the Catalina MCC (Figure 2, Arca & Johnson 2010), the exhumation response recorded by thermchronometry is relatively subdued. Apatite FT and AHe ages from the base of the Pirate Fault which offsets the Catalina detachment by ~2.6 km of vertical displacement (Davis et al. 2004), yield middle Miocene ages (17-11 Ma, Figure 2), consistent with the timing of Basin and Range extension in southern Arizona (~15-12 Ma, Dickinson 1991, Foster et al. 1993). Middle Miocene cooling ages are constrained to the lower temperature thermochronometers (AFT and AHe, Figure 5) and structurally deepest samples (Figure 6). Based on cooling through the AFT (T_C = 110 $\pm$ 10 °C) thermochronometer and a calculated paleogeothermal gradient of 25 °C/km, we assess that an upper limit of ~5 km of material was denuded by this latest phase of extension (Figure 4 and 5).

Basin and Range extension is attributed to oblique shear between the Pacific and American plates (e.g. Atwater 1970, Lerch et al. 2007, McQuarrie & Wernicke 2005). This allowed for the broadly synchronous onset of Basin and Range faulting and crustal thinning in the North American Cordillera (Dickinson 1991). In southern Arizona, the crustal thickness record suggests ~9 km of thinning between 20-10 Ma (~37 km) and present day (~28 km, Frassetto et al. 2006, Gilbert 2012) in contrast with the maximum of ~5 km of exhumation recorded by thermochronometers in the Catalina MCC (Figure 3). This record of thinning is consistent with geophysical evidence from Nevada, which estimated ~10 km of thinning between pre-Basin and Range (~40 km) and present day (~30 km Lerch et al. 2007, Gilbert 2012). Based

upon seismic imaging, upper- and lower-crustal Basin and Range deformation has been suggested to have been decoupled with no significant viscous transport of material via lower-crustal processes (Klemperer et al. 1986, Lerch et al. 2007). Thus, we suggest that Basin and Range crustal thinning was limited to upper-crustal processes (i.e. erosion or tectonic denudation) and higher temperature thermochronometric evidence is likely preserved at depth, beneath the current surface expression of the Catalina MCC (Figure 6C).

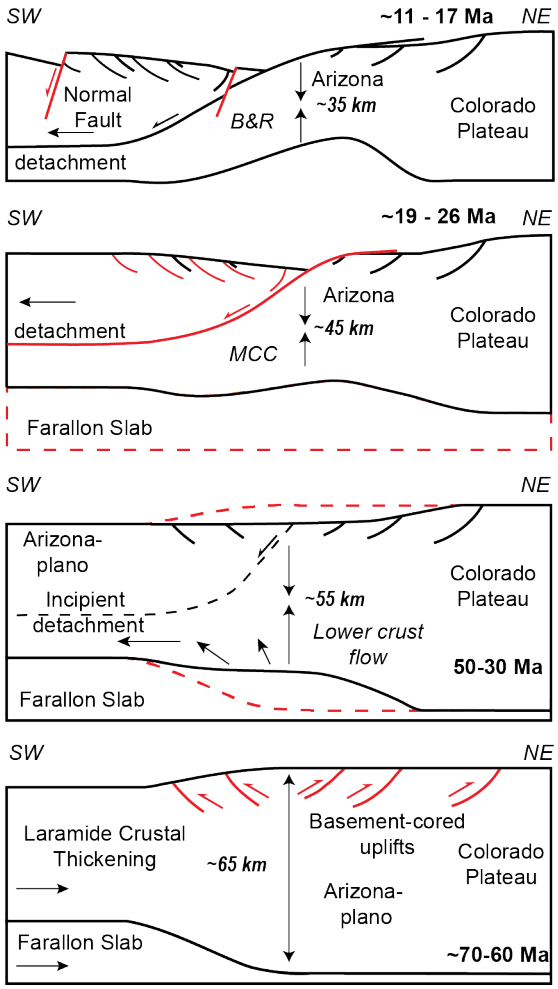

Figure 7: Schematic diagram illustrating the process of crustal thinning prior to detachment faulting and Basin and Range extension. Modified after Hyndman (2017).

5.1 Conclusions

In this study, we compare the exhumation history of the Catalina MCC as constrained by low-temperature thermochronometric data to the crustal thickness record as proxied by whole rock geochemistry to track thinning of an orogenic plateau. Thermochronometric data documents three discrete phases of cooling: a minor phase of upper-crustal cooling prior to *ca.* 40 Ma, associated with significant crustal thinning; a

major phase of cooling and crustal thinning between *ca.* 26-19 Ma related to detachment faulting and MCC exhumation, and a final phase of cooling and thinning at *ca.* 17-11 Ma related to Basin and Range extension. Using our thermochronological data-set as a proxy for denudation, we assess that $\leq$ 20 km of overburden was removed from the Catalina MCC via erosion or tectonic denudation associated with pre-MCC cooling, MCC detachment faulting, and Basin and Range extension. Geochemical evidence from plutonic rocks across southern Arizona support crustal thicknesses of ~60 $\pm$ 5 km at *ca.* 70-60 Ma which must have thinned by ~30 km to the present day thickness of ~28 km (e.g. Frassetto et al. 2006). Geochemical crustal thickness estimates from Sr/Y ratios of thinning are in broad agreement with denudation estimates from low-temperature thermochronology for the MCC and Basin and Range events. However, the amount of cooling during the Eocene from thermochronometric and structural evidence is insufficient to match thinning estimates obtained from geochemical evidence (~10km). Eocene cooling and crustal thinning corresponds spatially and temporally with ductile fabrics in the Catalina MCC, as well as with slower convergence between the Farallon and North American plates. Furthermore, Eocene extensional structures are not recognized in this locality. Since the Farallon slab was still in place below southern Arizona, we suggest that a phase of Eocene-Oligocene (*ca.* 50-30 Ma), middle- to lower-crustal ductile flow began to thin the Arizona-plano crust prior to Oligocene-Miocene extensional unroofing.

6 Acknowledgements

Tim Carter is thanked for the contribution of AFT data for the UoM samples obtained under Australian Research Council Grant DP0345931. Barbara Carrapa would like to acknowledge US National Science Foundation grant EAR Tectonics 1919179. Paul Kapp would like to acknowledge US National Science Foundation grant EAR 2048656. Jon Spencer is thanked for his invaluable support and guidance about the geology during fieldwork and valuable insights on an early draft. Asaf Raza provided assistance with sample preparation. The University of Melbourne Thermochronology Laboratory receives operation support through the AuScope program of the National Collaborative Research Infrastructure Strategy (NCRIS). We thank editor Isabelle Manighetti, the associate editor, reviewer M. Odlum, and an anonymous reviewer for their thoughtful comments which improved this manuscript.

Open Research

Data and figures supporting the conclusions presented here is available on the University of Arizona's Research Data Repository (https://doi.org/10.25422/azu.data.17227538.v1).

Figure Captions

Figure 1

Map of the south-western USA and north-western Mexico highlighting the "Nevada-plano" (purple dashed outline), "Arizona-plano" (black dashed outline), whole rock crustal thickness estimates and associated ages, and major shortening structures from Yonkee & Weil (2015). Modified after (Chapman et al. 2015, 2020). Estimated depth to mantle is from the Bouguer Gravity Anomaly (BGA, Gilbert 2012).

Figure 2

Geological map of the Catalina-Rincon metamorphic core complex (MCC) indicating major structures and units after (Arca & Johnson 2010), apatite fission-track (AFT), zircon fission-track (ZFT), apatite (U-Th-Sm)/He (AHe), and zircon (U-Th-Sm)/He (ZHe) ages from this study and (Jepson et al. 2021).

Figure 3

Sr/Y crustal thickness estimates from southern Arizona, eastern California, and western New Mexico through time. Box plots give the median crustal thickness estimate for each 10 myr interval and whiskers illustrate minimum and maximum constraints. Depth to Moho is analogous to crustal thickness. Blue line and grey envelope is mean spline and 1-standard error limit. Dashed line illustrates paucity of data constraining the 50-40 Ma time interval. Orange line is the convergence velocity between the Farallon and North American plates in mm per year from (Seton et al. 2012). Detailed sample information can be found in Supplementary File 4. Data points within each 10 myr bin have been separated to visualize crustal thickness estimate variation.

Figure 4

A) Representative thermal history model and paleo-geothermal gradient of the Catalina Metamorphic Core Complex indicating rapid cooling from temperatures of ~500-450 °C (e.g. Stipp et al. 2002) following

the best estimate for the onset of detachment faulting (Peters et al. 2003) and transitioning to relatively slower cooling during the Basin and Range. Green and purple dashed lines indicate the apatite partial retention zone and partial annealing zone, respectively (e.g. Braun et al. 2006). Samples used were from an elevation profile indicated in Figure 1, using apatite fission-track (AFT), apatite (U-Th-Sm)/He (AHe), and mean track length (MTL) data from this study and Jepson et al. (2021). Uncertainty on the paleo-geothermal estimate is indicated by the grey shading. Paleo-geothermal gradient decreases towards present day indicated by dashed line and outline at atmospheric temperature lapse rate of ~5-6 °C/km (Gallagher et al. 2005) and is unlikely to be an accurate estimate of the geothermal gradient. Modelling was performed using QTQt 5.7.0 (Gallagher 2012). B) Observed versus predicted values for all data used in the thermal history model. FT is fission-track and MTL is mean track length.

Figure 5

Kernel density estimates of combined zircon and apatite fission-track (ZFT, AFT) and zircon and apatite (U-Th-Sm)/He (ZHe and AHe) from this study, Fayon et al. (2000) and Jepson et al. (2021). The combined thermochronometers (temperatures from Braun et al. (2006)) constrain two major periods of cooling associated with the Basin and Range (11-17 Ma) and Metamorphic Core Complex (MCC, 19-26 Ma) events, and a minor, pre-MCC phase at *ca.* 40 Ma. Data-points are separated along the y-axis for visualization.

Figure 6

A) Cross-section of the Catalina Metamorphic Core Complex (MCC) indicating thermchronometric age versus elevation, with the projected Catalina detachment fault, ZFT = zircon fission-track, AFT = apatite fission-track, ZHe = zircon (U-Th)/He, and AHe = apatite (U-Th-Sm)/He. Cross-section shows no vertical exaggeration. Units are colored following Arca & Johnson (2010, and references therein). B) Plot displaying thermochronometric age against depth below the detachment. Depth to detachment was calculated by closest distance between sample locations and a 3D interpolation of the detachment surface constrained by surface exposure of the corrugated detachment surface. C) Plot displaying thermochronometric age against elevation. Break-in-slope at ~19 Ma identifies transition between rapid apparent exhumation (change in elevation/change in age) during MCC detachment faulting to slower exhumation during Basin and Range faulting. D) Geological map of the cross-sectioned area after Arca & Johnson (2010) showing locations of samples.

Figure 7

Schematic diagram illustrating the process of crustal thinning prior to detachment faulting and Basin and Range extension. Modified after Hyndman (2017).

Table Captions

Table 1

Samples collected from the Catalina-Rincon metamorphic core complex. Age is the reported crystallization age of the rock, “Lat" is the north latitude and “Long" is the east longitude using coordination system WSM 84, elevation (Elev) in meters above sea level. AFT is apatite fission-track, ZFT is zircon fission-track, AHe is apatite (U-Th-Sm)/He, and ZHe is zircon (U-Th-Sm)/He. Samples in italics are from Jepson et al. (2021).

Table 2

Apatite and zircon fission-track data from the Catalina metamorphic core complex. Samples in italics are from Jepson et al. (2021).

Table 3

Zircon (U-Th)/Helium data from the Catalina metamorphic core complex.

References

Arca, M. S. & Johnson, R. A. (2010), ‘Compilation Geologic Map from the Baboquivari Mountains to the Transition Zone of the Colorado Plateau’.
URL: *http://repository.azgs.az.gov/uri-gin/azgs/dlio/1377*

Atwater, T. (1970), ‘Implications of Plate Tectonics for the Cenozoic Tectonic Evolution of Western North America’, *GSA Bulletin* **81**(12), 3513–3536.
URL: *https://doi.org/10.1130/0016-7606(1970)81[3513:IOPTFT]2.0.CO;2*

Bahadori, A., Holt, W. E. & Rasbury, E. T. (2018), 'Reconstruction modeling of crustal thickness and paleotopography of western North America since 36 Ma', *Geosphere* **14**(3), 1207–1231.
URL: *https://doi.org/10.1130/GES01604.1*

Barton, M. D. (1990), Chapter 16: Cretaceous magmatism, metamorphism, and metallogeny in the east-central Great Basin, *in* 'The Nature and Origin of Cordilleran Magmatism', Geological Society of America.
URL: *https://doi.org/10.1130/MEM174-p283*

Best, M. G., Barr, D. L., Christiansen, E. H., Gromme, S., Deino, A. L. & Tingey, D. G. (2009), 'The Great Basin Altiplano during the middle Cenozoic ignimbrite flareup: insights from volcanic rocks', *International Geology Review* **51**(7-8), 589–633.
URL: *https://doi.org/10.1080/00206810902867690*

Best, M. G., Christiansen, E. H., de Silva, S. & Lipman, P. W. (2016), 'Slab-rollback ignimbrite flareups in the southern Great Basin and other Cenozoic American arcs: A distinct style of arc volcanism', *Geosphere* **12**(4), 1097–1135.
URL: *https://doi.org/10.1130/GES01285.1*

Bird, P. (1991), 'Lateral extrusion of lower crust from under high topography in the isostatic limit', *Journal of Geophysical Research: Solid Earth* **96**(B6), 10275–10286.
URL: *https://agupubs.onlinelibrary.wiley.com/doi/abs/10.1029/91JB00370*

Bird, P. (1998), 'Kinematic history of the Laramide orogeny in latitudes 3549 N, western United States', *Tectonics* **17**(5), 780–801.
URL: *https://agupubs.onlinelibrary.wiley.com/doi/abs/10.1029/98TC02698*

Botsyun, S., Sepulchre, P., Risi, C. & Donnadieu, Y. (2016), 'Impacts of Tibetan Plateau uplift on atmospheric dynamics and associated precipitation δ^{18}o', *Climate of the Past* **12**(6), 1401–1420.
URL: *https://cp.copernicus.org/articles/12/1401/2016/*

Braun, J., van der Beek, P. & Batt, G. (2006), *Quantitative thermochronology: numerical methods for the interpretation of thermochronological data*, Cambridge University Press.

Brown, R. W., Beucher, R., Roper, S., Persano, C., Stuart, F. & Fitzgerald, P. (2013), 'Natural age dispersion arising from the analysis of broken crystals. part i: Theoretical basis and implications for the

apatite (uth)/he thermochronometer', *Geochimica et Cosmochimica Acta* **122**, 478–497.
URL: *https://www.sciencedirect.com/science/article/pii/S0016703713003281*

Burchfiel, B. C., Cowan, D. S. & Davis, G. A. (1992), Tectonic overview of the Cordilleran orogen in the western United States, *in* 'The Cordilleran Orogen', Geological Society of America, pp. 407 – 480.
URL: *https://doi.org/10.1130/DNAG-GNA-G3.407*

Caylor, E. A., Carrapa, B., Sundell, K., DeCelles, P. G. & Smith, J. M. (2021), 'Age and deposition of the Fort Crittenden Formation: A window into Late Cretaceous Laramide and Cenozoic tectonics in southeastern Arizona', *GSA Bulletin* **133**(9-10), 1996–2016.
URL: *https://doi.org/10.1130/B35808.1*

Chapman, J. B., Ducea, M. N., DeCelles, P. G. & Profeta, L. (2015), 'Tracking changes in crustal thickness during orogenic evolution with Sr/Y: An example from the North American Cordillera', *Geology* **43**(10), 919–922.
URL: *https://doi.org/10.1130/G36996.1*

Chapman, J. B., Greig, R. & Haxel, G. B. (2020), 'Geochemical evidence for an orogenic plateau in the southern us and northern mexican cordillera during the laramide orogeny', *Geology* **48**(2), 164–168.

Chengfa, C., Nansheng, C., Coward, M. P., Wanming, D., Dewey, J. F., Gansser, A., Harris, N. B. W., Chengwei, J., Kidd, W. S. F., Leeder, M. R. et al. (1986), 'Preliminary conclusions of the Royal Society and Academia Sinica 1985 geotraverse of Tibet', *Nature* **323**(6088), 501–507.

Chiaradia, M. (2015), 'Crustal thickness control on Sr/Y signatures of recent arc magmas: an Earth scale perspective', *Scientific reports* **5**, 8115.

Coney, P. J. (1980), Cordilleran metamorphic core complexes: An overview, *in* 'Cordilleran Metamorphic Core Complexes', Geological Society of America.
URL: *https://doi.org/10.1130/MEM153-p7*

Coney, P. J. & Harms, T. A. (1984), 'Cordilleran metamorphic core complexes: Cenozoic extensional relics of mesozoic compression', *Geology* **12**(9), 550–554.

Coney, P. J. & Reynolds, S. J. (1977), 'Cordilleran benioff zones', *Nature* **270**(5636), 403–406.

Copeland, P., Currie, C. A., Lawton, T. F. & Murphy, M. A. (2017), 'Location, location, location: The variable lifespan of the Laramide orogeny', *Geology* **45**(3), 223–226.

Creasey, S. C., Banks, N. G., Ashley, R. P. & Theodore, T. G. (1976), Middle Tertiary plutonism in the Santa Catalina and Tortolita Mountains, Arizona, Technical report, U.S. Geological Survey. Report.
URL: *https://doi.org/10.3133/ofr76262*

Davis, G. A. (1988), 'Rapid upward transport of mid-crustal mylonitic gneisses in the footwall of a miocene detachment fault, whipple mountains, southeastern california', *Geologische Rundschau* **77**(1), 191–209.
URL: *https://doi.org/10.1007/BF01848684*

Davis, G. H. (1987), 'A shear-zone model for the structural evolution of metamorphic core complexes in southeastern arizona', *Geological Society, London, Special Publications* **28**(1), 247–266.
URL: *https://sp.lyellcollection.org/content/28/1/247*

Davis, G. H. (2013), 'Localization control for chlorite breccia deformation beneath Catalina detachment fault, Rincon Mountains, Tucson, Arizona', *Journal of Structural Geology* **50**, 237–253. Deformation localization in rocks.
URL: *https://www.sciencedirect.com/science/article/pii/S0191814112002726*

Davis, G. H. & Coney, P. J. (1979), 'Geologic development of the cordilleran metamorphic core complexes', *Geology* **7**(3), 120–124.

Davis, G. H., Constenius, K. N., Dickinson, W. R., Rodriguez, E. P. & Cox, L. J. (2004), 'Fault and fault-rock characteristics associated with Cenozoic extension and core-complex evolution in the Catalina-Rincon region, southeastern Arizona', *Geological Society of America Bulletin* **116**(1-2), 128–141.

Davis, G. H. & Hardy Jr., J. J. (1981), 'The Eagle Pass detachment, southeastern Arizona: Product of mid-Miocene listric (?) normal faulting in the southern Basin and Range', *Geological Society of America Bulletin* **92**(10), 749–762.

DeCelles, P. G. (2004), 'Late Jurassic to Eocene evolution of the Cordilleran thrust belt and foreland basin system, western USA', *American Journal of Science* **304**(2), 105–168.

DeCelles, P. G., Ducea, M. N., Kapp, P. & Zandt, G. (2009), 'Cyclicity in Cordilleran orogenic systems', *Nature Geoscience* **2**(4), 251–257.

Dickinson, W. R. (1991), Tectonic setting of faulted Tertiary strata associated with the Catalina core complex in southern Arizona, *in* 'Tectonic setting of faulted Tertiary strata associated with the Catalina

core complex in southern Arizona', Geological Society of America.
URL: *https://doi.org/10.1130/SPE264-p1*

Dickinson, W. R. (2004), 'Evolution of the North American Cordillera', *Annual Review of Earth and Planetary Sciences* **32**(1), 13–45.
URL: *https://doi.org/10.1146/annurev.earth.32.101802.120257*

Dickinson, W. R. & Snyder, W. S. (1978), Plate tectonics of the Laramide orogeny, *in* 'Laramide Folding Associated with Basement Block Faulting in the Western United States', Geological Society of America.
URL: *https://doi.org/10.1130/MEM151-p355*

Donelick, R. A., OSullivan, P. B. & Ketcham, R. A. (2005), 'Apatite Fission-Track Analysis', *Reviews in Mineralogy and Geochemistry* **58**(1), 49.
URL: *http://dx.doi.org/10.2138/rmg.2005.58.3*

Ducea, M. N., Triantafyllou, A. & Krcmaric, J. (2020), 'New Timing and Depth Constraints for the Catalina Metamorphic Core Complex, Southeast Arizona', *Tectonics* **39**(8), e2020TC006383. e2020TC006383 2020TC006383.
URL: *https://agupubs.onlinelibrary.wiley.com/doi/abs/10.1029/2020TC006383*

England, P. & McKenzie, D. (1982), 'A thin viscous sheet model for continental deformation', *Geophysical Journal International* **70**(2), 295–321.
URL: *https://doi.org/10.1111/j.1365-246X.1982.tb04969.x*

Enkelmann, E., Ratschbacher, L., Jonckheere, R., Nestler, R., Fleischer, M., Gloaguen, R., Hacker, B. R., Zhang, Y. Q. & Ma, Y.-S. (2006), 'Cenozoic exhumation and deformation of northeastern Tibet and the Qinling: Is Tibetan lower crustal flow diverging around the Sichuan Basin?', *GSA Bulletin* **118**(5-6), 651–671.
URL: *https://doi.org/10.1130/B25805.1*

Fan, M. & Carrapa, B. (2014), 'Late Cretaceousearly Eocene Laramide uplift, exhumation, and basin subsidence in Wyoming: Crustal responses to flat slab subduction', *Tectonics* **33**(4), 509–529.
URL: *https://agupubs.onlinelibrary.wiley.com/doi/abs/10.1002/2012TC003221*

Farley, K. A. (2002), '(U-Th)/He Dating: Techniques, Calibrations, and Applications', *Reviews in Mineralogy and Geochemistry* **47**(1), 819.
URL: *http://dx.doi.org/10.2138/rmg.2002.47.18*

Fayon, A. K., Peacock, S. M., Stump, E. & Reynolds, S. J. (2000), 'Fission track analysis of the footwall of the Catalina detachment fault, Arizona: Tectonic denudation, magmatism, and erosion', *Journal of Geophysical Research: Solid Earth* **105**(B5), 11047–11062.
URL: *https://agupubs.onlinelibrary.wiley.com/doi/abs/10.1029/1999JB900421*

Fitzgerald, P. G., Baldwin, S. L., Webb, L. E. & O'Sullivan, P. B. (2006), 'Interpretation of (UTh)/He single grain ages from slowly cooled crustal terranes: A case study from the Transantarctic Mountains of southern Victoria Land', *Chemical Geology* **225**(1), 91–120.
URL: *https://www.sciencedirect.com/science/article/pii/S0009254105003864*

Flowers, R. M., Ketcham, R. A., Shuster, D. L. & Farley, K. A. (2009), 'Apatite (UTh)/He thermochronometry using a radiation damage accumulation and annealing model', *Geochimica et Cosmochimica Acta* **73**(8), 2347–2365.
URL: *http://www.sciencedirect.com/science/article/pii/S001670370900043X*

Flowers, R., Shuster, D., Wernicke, B. & Farley, K. (2007), 'Radiation damage control on apatite (u-th)/he dates from the grand canyon region, colorado plateau', *Geology* **35**(5), 447–450.

Fornash, K. F., Patchett, P. J., Gehrels, G. E. & Spencer, J. E. (2013), 'Evolution of granitoids in the Catalina metamorphic core complex, southeastern Arizona: U–Pb, Nd, and Hf isotopic constraints', *Contributions to Mineralogy and Petrology* **165**(6), 1295–1310.

Foster, D. A., Gleadow, A. J. W., Reynolds, S. J. & Fitzgerald, P. G. (1993), 'Denudation of metamorphic core complexes and the reconstruction of the transition zone, west central arizona: Constraints from apatite fission track thermochronology', *Journal of Geophysical Research: Solid Earth* **98**(B2), 2167–2185.
URL: *https://agupubs.onlinelibrary.wiley.com/doi/abs/10.1029/92JB02407*

Frassetto, A., Gilbert, H., Zandt, G., Beck, S. & Fouch, M. J. (2006), 'Support of high elevation in the southern basin and range based on the composition and architecture of the crust in the basin and range and colorado plateau', *Earth and Planetary Science Letters* **249**(1), 62–73.
URL: *https://www.sciencedirect.com/science/article/pii/S0012821X06004833*

688 Gallagher, K. (2012), 'Transdimensional inverse thermal history modeling for quantitative thermochronol-
689 ogy', *Journal of Geophysical Research: Solid Earth* **117**(B2).
690 **URL:** *https://agupubs.onlinelibrary.wiley.com/doi/abs/10.1029/2011JB008825*

691 Gallagher, K., Stephenson, J., Brown, R., Holmes, C. & Fitzgerald, P. (2005), 'Low temperature ther-
692 mochronology and modeling strategies for multiple samples 1: Vertical profiles', *Earth and Planetary*
693 *Science Letters* **237**(1), 193–208.
694 **URL:** *https://www.sciencedirect.com/science/article/pii/S0012821X05004085*

695 Gerbault, M., Martinod, J. & Hérail, G. (2005), 'Possible orogeny-parallel lower crustal flow and thickening
696 in the Central Andes', *Tectonophysics* **399**(1), 59–72. Andean Geodynamics:.
697 **URL:** *https://www.sciencedirect.com/science/article/pii/S0040195105000168*

698 Gerin, C., Gautheron, C., Oliviero, E., Bachelet, C., Mbongo Djimbi, D., Seydoux-Guillaume, A.-M.,
699 Tassan-Got, L., Sarda, P., Roques, J. & Garrido, F. (2017), 'Influence of vacancy damage on He dif-
700 fusion in apatite, investigated at atomic to mineralogical scales', *Geochimica et Cosmochimica Acta*
701 **197**, 87–103.
702 **URL:** *https://www.sciencedirect.com/science/article/pii/S0016703716305956*

703 Gilbert, H. (2012), 'Crustal structure and signatures of recent tectonism as influenced by ancient terranes
704 in the western United States', *Geosphere* **8**(1), 141–157.
705 **URL:** *https://doi.org/10.1130/GES00720.1*

706 Gleadow, A. J. W., , A. J. H. & Quaife, R. D. (1976), 'Fission track dating of zircon: Improved etching
707 techniques', *Earth and Planetary Science Letters* **33**(2), 273–276.
708 **URL:** *https://www.sciencedirect.com/science/article/pii/0012821X76902351*

709 Gleadow, A. J. W., Harrison, M., Kohn, B. P., Lugo-Zazueta, R. & Phillips, D. (2015), 'The Fish Canyon
710 Tuff: A new look at an old low-temperature thermochronology standard', *Earth and Planetary Science*
711 *Letters* **424**, 95 – 108.
712 **URL:** *http://www.sciencedirect.com/science/article/pii/S0012821X15002927*

713 Gottardi, R., McAleer, R., Casale, G., Borel, M., Iriondo, A. & Jepson, G. (2020), 'Exhumation of the coy-
714 ote mountains metamorphic core complex (arizona): Implications for orogenic collapse of the southern
715 north american cordillera', *Tectonics* **39**(8), e2019TC006050. e2019TC006050 2019TC006050.
716 **URL:** *https://agupubs.onlinelibrary.wiley.com/doi/abs/10.1029/2019TC006050*

Humphreys, E. (2009), 'Relation of flat subduction to magmatism and deformation in the western United States', *Backbone of the Americas: Shallow subduction, plateau uplift, and ridge and terrane collision* **204**, 85.

Hurford, A. J. & Green, P. F. (1983), 'The zeta age calibration of fission-track dating', *Chemical Geology* **41**, 285 – 317.
URL: *http://www.sciencedirect.com/science/article/pii/S0009254183800266*

Hyndman, R. (2017), 'Lower-crustal flow and detachment in the North American Cordillera: a consequence of Cordillera-wide high temperatures', *Geophysical Journal International* **209**(3), 1779–1799.
URL: *https://doi.org/10.1093/gji/ggx138*

Jacobson, C. E., Grove, M., Vucic, A., Pedrick, J. N. & Ebert, K. A. (2007), Exhumation of the Orocopia Schist and associated rocks of southeastern California: Relative roles of erosion, synsubduction tectonic denudation, and middle Cenozoic extension, *in* 'Convergent Margin Terranes and Associated Regions: A Tribute to W.G. Ernst', Geological Society of America.
URL: *https://doi.org/10.1130/2007.2419(01)*

Jepson, G., Carrapa, B., George, S., Triantafyllou, A., Egan, S., Constenius, K., Gehrels, G. & Ducea, M. (2021), 'Resolving mid- to upper-crustal exhumation through apatite petrochronology and thermochronology', *Chemical Geology* **565**, 120071.
URL: *https://www.sciencedirect.com/science/article/pii/S0009254121000152*

Ketcham, R. A. (1996), 'Distribution of heat-producing elements in the upper and middle crust of southern and west central arizona: Evidence from the core complexes', *Journal of Geophysical Research: Solid Earth* **101**(B6), 13611–13632.
URL: *https://agupubs.onlinelibrary.wiley.com/doi/abs/10.1029/96JB00664*

Ketcham, R. A., Carter, A., Donelick, R. A., Barbarand, J. & Hurford, A. J. (2007), 'Improved modeling of fission-track annealing in apatite', *American Mineralogist* **92**(5-6), 799.
URL: *http://dx.doi.org/10.2138/am.2007.2281*

Klemperer, S. L., Hauge, T. A., Hauser, E. C., Oliver, J. E. & Potter, C. J. (1986), 'The Moho in the northern Basin and Range province, Nevada, along the COCORP 40 N seismic-reflection transect', *GSA Bulletin* **97**(5), 603–618.
URL: *https://doi.org/10.1130/0016-7606(1986)97<603:TMITNB>2.0.CO;2*

Lavier, L. L. & Manatschal, G. (2006), 'A mechanism to thin the continental lithosphere at magma-poor margins', *Nature* **440**(7082), 324–328.
URL: *https://doi.org/10.1038/nature04608*

Lee, C.-T. A. & Morton, D. M. (2015), 'High silica granites: Terminal porosity and crystal settling in shallow magma chambers', *Earth and Planetary Science Letters* **409**, 23–31.
URL: *https://www.sciencedirect.com/science/article/pii/S0012821X14006670*

Lerch, D. W., Klemperer, S. L., Glen, J. M. G., Ponce, D. A., Miller, E. L. & Colgan, J. P. (2007), 'Crustal structure of the northwestern Basin and Range Province and its transition to unextended volcanic plateaus', *Geochemistry, Geophysics, Geosystems* **8**(2).
URL: *https://agupubs.onlinelibrary.wiley.com/doi/abs/10.1029/2006GC001429*

Lister, G. S. & Davis, G. A. (1989), 'The origin of metamorphic core complexes and detachment faults formed during Tertiary continental extension in the northern Colorado River region, U.S.A.', *Journal of Structural Geology* **11**(1), 65 – 94.
URL: *http://www.sciencedirect.com/science/article/pii/0191814189900369*

Liu, L., Gurnis, M., Seton, M., Saleeby, J., Müller, D. R. & Jackson, J. M. (2010), 'The role of oceanic plateau subduction in the Laramide orogeny', *Nature Geoscience* **3**(5), 353–357.

Livaccari, R. F. (1991), 'Role of crustal thickening and extensional collapse in the tectonic evolution of the Sevier-Laramide orogeny, western United States', *Geology* **19**(11), 1104–1107.
URL: *https://doi.org/10.1130/0091-7613(1991)019<1104:ROCTAE>2.3.CO;2*

Long, K. B., Gehrels, G. E. & Baldwin, S. L. (1995), 'Tectonothermal evolution of the Pinaleno-Jackson Mountain core complex, southeast Arizona', *GSA Bulletin* **107**(10), 1231–1240.
URL: *https://doi.org/10.1130/0016-7606(1995)107<1231:TEOTPO>2.3.CO;2*

Mantle, G. W. & Collins, W. J. (2008), 'Quantifying crustal thickness variations in evolving orogens: Correlation between arc basalt composition and Moho depth', *Geology* **36**(1), 87–90.
URL: *https://doi.org/10.1130/G24095A.1*

McDowell, F. W., McIntosh, W. C. & Farley, K. A. (2005), 'A precise 40Ar39Ar reference age for the Durango apatite (UTh)/He and fission-track dating standard', *Chemical Geology* **214**(3), 249 – 263.
URL: *http://www.sciencedirect.com/science/article/pii/S0009254104004218*

McKenzie, D. & Jackson, J. (2002), 'Conditions for flow in the continental crust', *Tectonics* **21**(6), 51–57.
URL: *https://agupubs.onlinelibrary.wiley.com/doi/abs/10.1029/2002TC001394*

McQuarrie, N. & Wernicke, B. P. (2005), 'An animated tectonic reconstruction of southwestern North America since 36 Ma', *Geosphere* **1**(3), 147–172.
URL: *https://doi.org/10.1130/GES00016.1*

Molnar, P., Boos, W. R. & Battisti, D. S. (2010), 'Orographic controls on climate and paleoclimate of asia: Thermal and mechanical roles for the tibetan plateau', *Annual Review of Earth and Planetary Sciences* **38**(1), 77–102.
URL: *https://doi.org/10.1146/annurev-earth-040809-152456*

Moser, A. C., Ault, A. K., Stearns, M. A., Evans, J. P. & Guenthner, W. R. (2021), 'Late OligoceneEarly Miocene Detachment Faulting in Crystalline Basement, Mecca Hills, CA, Documented With Zircon (UTh)/He Date-eU-Visual Radiation Damage Patterns', *Tectonics* **40**(9), e2021TC006809. e2021TC006809 2021TC006809.
URL: *https://agupubs.onlinelibrary.wiley.com/doi/abs/10.1029/2021TC006809*

Oldow, J. S., Bally, A. W., Lallemant, H. G. A. & Leeman, W. P. (1989), Phanerozoic evolution of the North American Cordillera; United States and Canada, *in* 'The Geology of North AmericaAn Overview', Geological Society of America.
URL: *https://doi.org/10.1130/DNAG-GNA-A.139*

Peters, L., Ferguson, C. A., Spencer, J. E., Orr, T. R. & Dickinson, W. R. (2003), 'Sixteen $^{40}Ar/^{39}Ar$ geochronology analyses from southeastern Arizona', *Arizona Geological Survey Open File Report* p. 46.

Peyton, L. S. & Carrapa, B. (2013), An overview of low-temperature thermochronology in the Rocky Mountains and its application to petroleum system analysis, *in* C. Knight & J. Cuzella, eds, 'Application of structural methods to Rocky Mountain hydrocarbon exploration and development, AAPG Studies in Geology', Vol. 65, AAPG Special Volumes, pp. 37–70.

Platt, J. P., Behr, W. M. & Cooper, F. J. (2015), 'Metamorphic core complexes: windows into the mechanics and rheology of the crust', *Journal of the Geological Society* **172**(1), 9–27.
URL: *https://jgs.lyellcollection.org/content/172/1/9*

Reiners, P. W. (2005), 'Zircon (U-Th)/He Thermochronometry', *Reviews in Mineralogy and Geochemistry* **58**(1), 151–179.
URL: *https://doi.org/10.2138/rmg.2005.58.6*

Rey, P., Teyssier, C. & Whitney, D. (2009), 'The role of partial melting and extensional strain rates in the development of metamorphic core complexes', *Tectonophysics* **477**(3), 135 – 144. Hot orogens.
URL: *http://www.sciencedirect.com/science/article/pii/S0040195109001619*

Riley, B. C. D. (2004), *Laramide exhumation and heating in southeastern Arizona: low-temperature thermal history and implications for zircon fission-track systematics*, The University of Texas at Austin.

Rønnevik, C., Ksienzyk, A. K., Fossen, H. & Jacobs, J. (2017), 'Thermal evolution and exhumation history of the Uncompahgre Plateau (northeastern Colorado Plateau), based on apatite fission track and (U-Th)-He thermochronology and zircon U-Pb dating', *Geosphere* **13**(2), 518–537.

Royden, L. H., Burchfiel, B. C., King, R. W., Wang, E., Chen, Z., Shen, F. & Liu, Y. (1997), 'Surface Deformation and Lower Crustal Flow in Eastern Tibet', *Science* **276**(5313), 788–790.
URL: *https://science.sciencemag.org/content/276/5313/788*

Ruddiman, W. F. & Kutzbach, J. E. (1991), 'Plateau uplift and climatic change', *Scientific American* **264**(3), 66–75.
URL: *http://www.jstor.org/stable/24936829*

Saleeby, J. (2003), 'Segmentation of the Laramide Slabevidence from the southern Sierra Nevada region', *GSA Bulletin* **115**(6), 655–668.
URL: *https://doi.org/10.1130/0016-7606(2003)115<0655:SOTLSF>2.0.CO;2*

Say, M. C. & Zuza, A. V. (2021), 'Heterogenous late Miocene extension in the northern Walker Lane (California-Nevada, USA) demonstrates vertically decoupled crustal extension', *Geosphere* .
URL: *https://doi.org/10.1130/GES02409.1*

Schildgen, T. F., Cosentino, D., Bookhagen, B., Niedermann, S., Yldrm, C., Echtler, H., Wittmann, H. & Strecker, M. R. (2012), 'Multi-phased uplift of the southern margin of the central anatolian plateau, turkey: A record of tectonic and upper mantle processes', *Earth and Planetary Science Letters* **317-318**, 85–95.
URL: *https://www.sciencedirect.com/science/article/pii/S0012821X11007175*

Schutt, D. L., Lowry, A. R. & Buehler, J. S. (2018), 'Moho temperature and mobility of lower crust in the western United States', *Geology* **46**(3), 219–222.
URL: *https://doi.org/10.1130/G39507.1*

Scoggin, S. H., Chapman, J. B., Shields, J. E., Trzinski, A. E. & Ducea, M. N. (2021), 'Early Paleogene Magmatism in the Pinaleño Mountains, Arizona: Evidence for Crustal Melting of Diverse Basement Assemblages during the Laramide Orogeny', *Journal of Petrology* **62**(12). egab095.
URL: *https://doi.org/10.1093/petrology/egab095*

Seton, M., Müller, R., Zahirovic, S., Gaina, C., Torsvik, T., Shephard, G., Talsma, A., Gurnis, M., Turner, M., Maus, S. & Chandler, M. (2012), 'Global continental and ocean basin reconstructions since 200 Ma', *Earth-Science Reviews* **113**(3), 212–270.
URL: *https://www.sciencedirect.com/science/article/pii/S0012825212000311*

Shuster, D. L., Flowers, R. M. & Farley, K. A. (2006), 'The influence of natural radiation damage on helium diffusion kinetics in apatite', *Earth and Planetary Science Letters* **249**(3), 148–161.
URL: *https://www.sciencedirect.com/science/article/pii/S0012821X0600519X*

Singleton, J. S., Seymour, N. M., Reynolds, S. J., Vomocil, T. & Wong, M. S. (2019), 'Distributed Neogene faulting across the western to central Arizona metamorphic core complex belt: Synextensional constriction and superposition of the PacificNorth America plate boundary on the southern Basin and Range', *Geosphere* **15**(4), 1409–1435.
URL: *https://doi.org/10.1130/GES02036.1*

Singleton, J. S., Wong, M. S. & Johnston, S. M. (2018), 'The role of calcite-rich metasedimentary mylonites in localizing detachment fault strain and influencing the structural evolution of the Buckskin-Rawhide metamorphic core complex, west-central Arizona', *Lithosphere* **10**(2), 172–193.
URL: *https://doi.org/10.1130/L699.1*

Snyder, W., Dickinson, W. & Silberman, M. (1976), 'Tectonic implications of space-time patterns of Cenozoic magmatism in the western United States', *Earth and Planetary Science Letters* **32**(1), 91–106.
URL: *https://www.sciencedirect.com/science/article/pii/0012821X76901898*

Sonder, L. J. & Jones, C. H. (1999), 'Western United States Extension: How the West was Widened', *Annual Review of Earth and Planetary Sciences* **27**(1), 417–462.
URL: *https://doi.org/10.1146/annurev.earth.27.1.417*

Spencer, J. E. & Reynolds, S. J. (1989), 'Middle Tertiary tectonics of Arizona and adjacent areas', *Geologic evolution of Arizona: Arizona Geological Society Digest* **17**, 539–574.

Spencer, J. E., Richard, S. M., Lingrey, S. H., Johnson, B. J., Johnson, R. A. & Gehrels, G. E. (2019), 'Reconstruction of Mid-Cenozoic Extension in the Rincon Mountains Area, Southeastern Arizona, USA, and Geodynamic Implications', *Tectonics* **38**(7), 2338–2357.
URL: *https://agupubs.onlinelibrary.wiley.com/doi/abs/10.1029/2019TC005565*

Spiegel, C., Kohn, B. P., Belton, D., Berner, Z. & Gleadow, A. J. W. (2009), 'Apatite (UThSm)/He thermochronology of rapidly cooled samples: The effect of He implantation', *Earth and Planetary Science Letters* **285**(1), 105–114.
URL: *https://www.sciencedirect.com/science/article/pii/S0012821X0900332X*

Stipp, M., Stünitz, H., Heilbronner, R. & Schmid, S. M. (2002), 'The eastern Tonale fault zone: a natural laboratory for crystal plastic deformation of quartz over a temperature range from 250 to 700řC', *Journal of Structural Geology* **24**(12), 1861–1884.
URL: *https://www.sciencedirect.com/science/article/pii/S0191814102000354*

Terrien, J. J. (2012), The role of magmatism in the Catalina metamorphic core complex, Arizona: insights from integrated thermochronology, gravity and aeromagnetic data, PhD thesis, Syracuse University.

Thacker, J. O., Kelley, S. A. & Karlstrom, K. E. (2021), 'Late CretaceousRecent Low-Temperature Cooling History and Tectonic Analysis of the Zuni Mountains, West-Central New Mexico', *Tectonics* **40**(4), e2020TC006643. e2020TC006643 2020TC006643.
URL: *https://agupubs.onlinelibrary.wiley.com/doi/abs/10.1029/2020TC006643*

Wells, M. L. & Hoisch, T. D. (2008), 'The role of mantle delamination in widespread Late Cretaceous extension and magmatism in the Cordilleran orogen, western United States', *GSA Bulletin* **120**(5-6), 515–530.
URL: *https://doi.org/10.1130/B26006.1*

Wernicke, B. (1990), The Fluid Crustal Layer and Its Implications for Continental Dynamics, *in* M. H. Salisbury & D. M. Fountain, eds, 'Exposed Cross-Sections of the Continental Crust', Springer Netherlands, Dordrecht, pp. 509–544.
URL: *https://doi.org/10.1007/978-94-009-0675-4-21*

Whitney, D. L., Teyssier, C., Rey, P. & Buck, W. R. (2013), 'Continental and oceanic core complexes', *GSA Bulletin* **125**(3-4), 273–298.
URL: *https://doi.org/10.1130/B30754.1*

Wildman, M., Brown, R., Beucher, R., Persano, C., Stuart, F., Gallagher, K., Schwanethal, J. & Carter, A. (2016), 'The chronology and tectonic style of landscape evolution along the elevated Atlantic continental margin of South Africa resolved by joint apatite fission track and (U-Th-Sm)/He thermochronology', *Tectonics* **35**(3), 511–545.
URL: *https://agupubs.onlinelibrary.wiley.com/doi/abs/10.1002/2015TC004042*

Winn, C., Karlstrom, K. E., Shuster, D. L., Kelley, S. & Fox, M. (2017), '6 Ma age of carving Westernmost Grand Canyon: Reconciling geologic data with combined AFT, (UTh)/He, and 4He/3He thermochronologic data', *Earth and Planetary Science Letters* **474**, 257–271.
URL: *https://www.sciencedirect.com/science/article/pii/S0012821X17303758*

Wong, M. S. & Gans, P. B. (2008), 'Geologic, structural, and thermochronologic constraints on the tectonic evolution of the Sierra Mazatán core complex, Sonora, Mexico: New insights into metamorphic core complex formation', *Tectonics* **27**(4).
URL: *https://agupubs.onlinelibrary.wiley.com/doi/abs/10.1029/2007TC002173*

Wright, N. M., Seton, M., Williams, S. E. & Müller, D. R. (2016), 'The Late Cretaceous to recent tectonic history of the Pacific Ocean basin', *Earth-Science Reviews* **154**, 138–173.
URL: *https://www.sciencedirect.com/science/article/pii/S001282521530074X*

Wu, G., Duan, A., Liu, Y., Mao, J., Ren, R., Bao, Q., He, B., Liu, B. & Hu, W. (2014), 'Tibetan Plateau climate dynamics: recent research progress and outlook', *National Science Review* **2**(1), 100–116.
URL: *https://doi.org/10.1093/nsr/nwu045*

Yonkee, W. A. & Weil, A. B. (2015), 'Tectonic evolution of the Sevier and Laramide belts within the North American Cordillera orogenic system', *Earth-Science Reviews* **150**, 531 – 593.
URL: *http://www.sciencedirect.com/science/article/pii/S0012825215300258*

Zeitler, P. K., Enkelmann, E., Thomas, J. B., Watson, E. B., Ancuta, L. D. & Idleman, B. D. (2017), 'Solubility and trapping of helium in apatite', *Geochimica et Cosmochimica Acta* **209**, 1–8.
URL: *https://www.sciencedirect.com/science/article/pii/S0016703717302028*

Zhong, S. (1997), ‘Dynamics of crustal compensation and its influences on crustal isostasy’, *Journal of Geophysical Research: Solid Earth* **102**(B7), 15287–15299.
URL: *https://agupubs.onlinelibrary.wiley.com/doi/abs/10.1029/97JB00956*